AGU PUBLICATIONS

Water Resources Research

RESEARCH ARTICLE

10.1002/2017WR020827

Modeling Subsurface Hydrology in Floodplains

Cristina M. Evans[1,2], David G. Dritschel[2], and Michael B. Singer[3,4]

[1]School of Earth and Environmental Sciences, University of St Andrews, St Andrews, UK, [2]School of Mathematics and Statistics, University of St Andrews, St Andrews, UK, [3]School of Earth and Ocean Sciences, Cardiff University, Cardiff, UK, [4]Earth Research Institute, University of California Santa-Barbara, Santa Barbara, CA, USA

Key Points:
- Floodplains can have complex patterns of soil-moisture due to infiltration/evaporation and subsurface river flux
- We developed a model that links these processes to assess moisture patterns at chosen depths and floodplain locations
- This model can be used to assess water availability to vegetation over rooting depths at any distance from the channel

Correspondence to:
C. M. Evans,
cme7@st-andrews.ac.uk

Citation:
Evans, C. M., Dritschel, D. G., & Singer, M. B. (2018). Modeling subsurface hydrology in floodplains. *Water Resources Research*, *54*. https://doi.org/10.1002/2017WR020827

Received 30 MAR 2017
Accepted 24 JAN 2018
Accepted article online 30 JAN 2018

Abstract Soil-moisture patterns in floodplains are highly dynamic, owing to the complex relationships between soil properties, climatic conditions at the surface, and the position of the water table. Given this complexity, along with climate change scenarios in many regions, there is a need for a model to investigate the implications of different conditions on water availability to riparian vegetation. We present a model, HaughFlow, which is able to predict coupled water movement in the vadose and phreatic zones of hydraulically connected floodplains. Model output was calibrated and evaluated at six sites in Australia to identify key patterns in subsurface hydrology. This study identifies the importance of the capillary fringe in vadose zone hydrology due to its water storage capacity and creation of conductive pathways. Following peaks in water table elevation, water can be stored in the capillary fringe for up to months (depending on the soil properties). This water can provide a critical resource for vegetation that is unable to access the water table. When water table peaks coincide with heavy rainfall events, the capillary fringe can support saturation of the entire soil profile. HaughFlow is used to investigate the water availability to riparian vegetation, producing daily output of water content in the soil over decadal time periods within different depth ranges. These outputs can be summarized to support scientific investigations of plant-water relations, as well as in management applications.

1. Introduction

The vadose zone is a region of unsaturated soil, vertically bounded by the land surface and the water table. This zone is an important pathway controlling water exchange between surface water and groundwater in the hydrological cycle. It buffers hydrologic extremes, such as floods and droughts by storing water and modulating its movement (Harter & Hopmans, 2004). It also provides a critical moisture source for local ecosystem functioning (van Genuchten, 1991). However, the dependence of these ecosystems on groundwater hydrology is poorly understood (Rohde et al., 2017).

Riparian environments have especially complex hydrology due to the joint contribution of vertical processes (precipitation, evaporation, and capillary rise) and lateral processes (subsurface hyporheic flow). With streambed connection, river water feeds into the floodplain's phreatic zone (the saturated zone underlying the vadose zone). This water influx provides a crucial resource for water-limited vegetation (Snyder & Williams, 2000; Williams et al., 2006). Water-stressed riparian vegetation is particularly sensitive to changes in soil-moisture (Sargeant & Singer, 2016; Singer et al., 2014, 2013; Snyder & Williams, 2000; Williams et al., 2006). Hence, it is important to understand how climate is expressed in subsurface hydrology to predict the impact of future climatic trends on riparian ecosystems. Spatial and temporal variations in soil-moisture, driven by direct local climate (i.e., precipitation and evaporation) and indirect nonlocal climate (manifesting as riverine process), should be studied both individually, as decoupled units, and in tandem. Modeling the effects of each process can allow us to decipher patterns of water availability to vegetation, which is especially important in light of the fact that there are open questions about which water sources plants use (Evaristo et al., 2015; Sprenger et al., 2016).

Surface hydrology, i.e., precipitation and river discharge regimes, is extensively both monitored and modeled. Surface models play an essential role in water management schemes (Singh & Woolhiser, 2002). However, as soil-moisture can be costly to measure at high spatial and temporal resolution, the complex relationships between subsurface processes can be more-easily investigated using physically based

mathematical models. Generally, we can expect infiltrating precipitation to move downward through the soil and hyporheic flow to supply the water table laterally, but modeling is needed to understand their interplay and temporal legacy on soil-moisture patterns. This interplay is important because it can generate water stores for riparian vegetation with particular water demands and rooting depths (Canham et al., 2012; Singer et al., 2014). The residence times of these stores determine the moisture availability in the soil during drought conditions, yet water content at any particular soil depth is difficult to predict without numerical simulations. Models also provide the flexibility to quickly and economically analyze large time intervals with high spatial and temporal resolution.

A variety of models with varying complexity exist to simulate subsurface hydrology; from data-driven/stochastic to physically/process-based models. These models are created for a range of different purposes and are made available open-source or as commercial products. Some of the most commonly used hydrology models include HydroGeoSphere (Therrien et al., 2010), HYDRUS 3D (Šimůnek et al., 2008), MIKE SHE (Refsgaard & Storm, 1995), MODFLOW (Harbaugh et al., 2000), and ParFlow (Maxwell et al., 2016). The main differences between these models are the formulation of the governing equations, their coupling, the boundary conditions, and their spatial and temporal discretization (Maxwell et al., 2014). Differences also arise in the chosen dimensionality of each equation used; groundwater flow can be simulated in one or two dimensions and the infiltration Richards' equation can be simulated in up to three dimensions.

The scientific community has questioned the increasing number of models being produced in this field. Baird and Wilby (1999) discuss the needless pursuit of new model solutions in ecohydrology when good solutions already exist. The authors agree that it would be ideal to progress with existing models; however, the widely used available models are large and complex, making it hard to gain a full understanding of the limitations and assumptions involved. In developing a model specific to our intended application, we are able to ensure that the model is as accurate and efficient as possible, and is constructed in a way that is suitable for simulating the processes involved.

In this paper, we introduce HaughFlow, a light-weight, flexible model which couples the one-dimensional Richards equation (Richards, 1931) for vertical moisture transport, with the Boussinesq equation (Boussinesq, 1904) for lateral saturated flow perpendicular to the river channel. HaughFlow is a modern, more flexible version of the Pikul et al. (1974) model, with an optimization procedure for calibrating key parameters and capability for a range of output data visualizations. HaughFlow requires minimal inputs, ensuring model application is as simple as possible. The simplicity of the model structure allows us to investigate the roles of each subsurface flow component, and to specifically identify the influence of a shallow hyporheic-dominated water table on patterns of soil-water saturation throughout the vadose zone. HaughFlow assumes lateral hyporheic flow is the dominant driver of water table levels in the riparian corridor; the model is thus applicable to floodplains where the river and groundwater are hydraulically connected. A source/sink term in the Boussinesq equation, as described by Zucker et al. (1973) and Pikul et al. (1974), is used to fully represent the interplay between the vadose and phreatic zones. This term allows the soil-moisture conditions in the vadose zone to influence water table dynamics. A capillary fringe, induced by boundary conditions at the water table, allows for water table contributions to soil-moisture in the vadose zone.

Numerical simulations are presented using the HaughFlow model to investigate the role of hydroclimate in controlling water content and fluxes at all subsurface depths down to the floodplain water table. After evaluating the model against piezometer data, we apply the model over decadal time scales along a floodplain transect in the Murray-Darling basin, Australia, using existing data on climate, soil parameters, and river stage. We obtain daily output from HaughFlow to explore the subsurface moisture and flow responses to seasonally and annually varying boundary conditions. We use these output data to quantify the lateral expression of water table dynamics within the floodplain, as well as to identify the impact of water table fluctuations on deep soil-moisture.

2. Model Structure and Components

HaughFlow, after the Scottish "Haugh" for the flat alluvial land by a river, is a physically based numerical model constructed to be flexible, user-friendly, and with a simplistic composition. The soil and computational parameters can be easily adapted, along with the depth and position of the simulated area, to suit

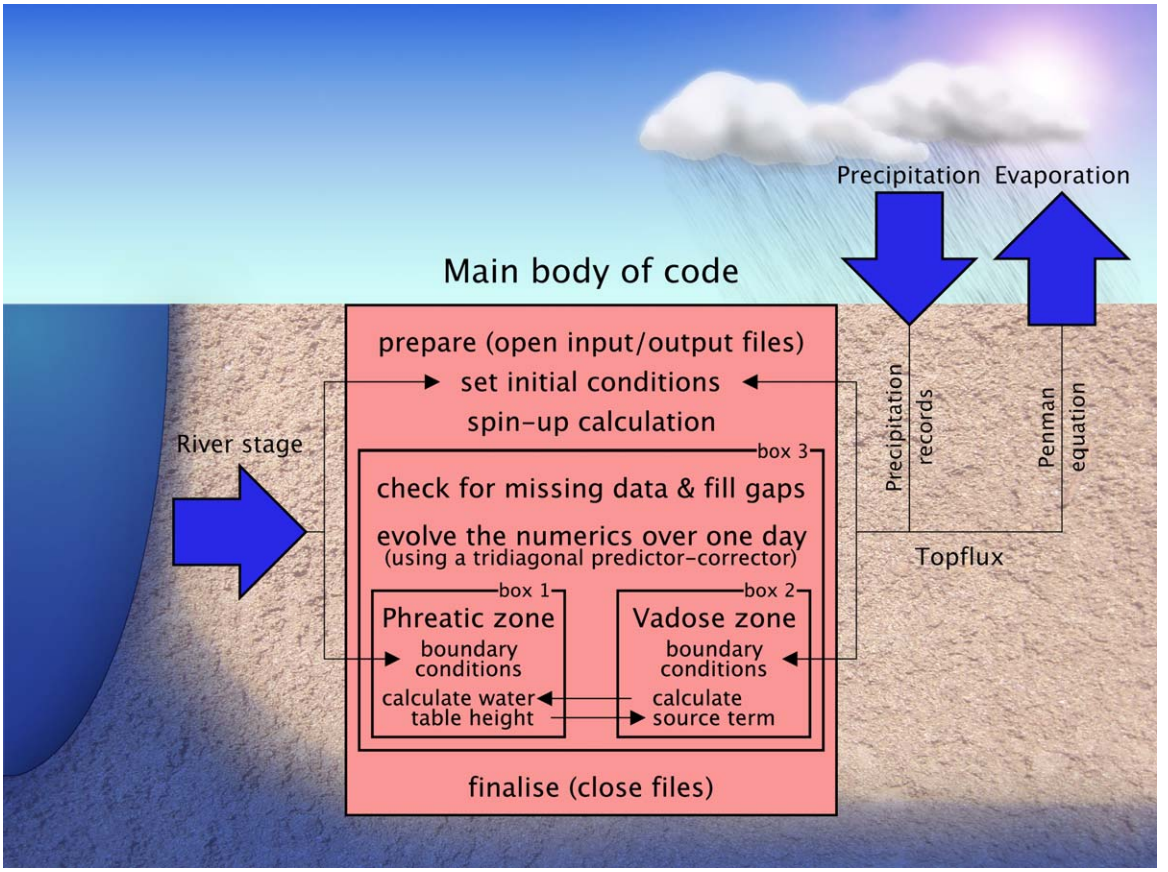

Figure 1. Structure of HaughFlow, the model created for this study. Box 1 shows the calculation of the water table or the extent of the phreatic zone, with river stage records as input to the Boussinesq equation and the water table height feeding into the vadose zone calculation. Box 2 is the vadose zone component of the model, calculated using precipitation and evaporation inputs to the Richards equation. Upon completion of the Richards calculation, the source term in the Boussinesq equation is evaluated and fed across. Box 3 shows the section of the model which is looped over each day, Boxes 1 and 2 are looped over each time step.

the user's experimental scope and scale of interest. HaughFlow constitutes the minimum processes required to simulate water movement.

The components and structure of HaughFlow are outlined in Figure 1. The structure reflects that of the soil region it simulates, with separate modules defining each of the input fluxes that feed into the vertical Richards and horizontal Boussinesq components. Each component has its own boundary conditions, initial conditions, and spatial step, however they share a common time step. The surface input fluxes comprise precipitation and evapotranspiration, and are incorporated through the upper boundary condition. This is read into the main body of the code that calculates internal vertical infiltration and diffusion. Horizontally, the water table position is determined by calculating the hyporheic exchange flow, and assimilated through a lower boundary coupling with the vertical infiltration equation. An accurate tridiagonal solver along with a predictor-corrector scheme (as in Pikul et al., 1974) is used for the temporal discretization, and centered finite differences are used for the spatial discretization (see Appendix A for details).

2.1. Infiltration and Diffusion Component

The vertical transport of moisture in the vadose zone is modeled using the Richards (1931) equation. This equation combines Darcy's law (1856) for vertical unsaturated flow and the principle of conservation of mass, leading to the following evolution equation for the hydraulic pressure head ψ (L),

$$C(\psi)\frac{\partial \psi}{\partial t} = \frac{\partial}{\partial z}\left(K(\psi)\left(\frac{\partial \psi}{\partial z} + 1\right)\right), \tag{1}$$

where z (L) is the vertical coordinate (measured upward), K (L/T) is the effective hydraulic conductivity, t is time, and C (1/L) is the specific moisture capacity defined below. A substitution of $\zeta = -\psi$ is then made to yield positive ζ values above the water table. Applying this substitution to equation (1) gives

$$C\ \frac{\partial \zeta}{\partial t} = \frac{\partial}{\partial z}\left(K\left(\frac{\partial \zeta}{\partial z} - 1\right)\right), \tag{2}$$

where C is defined by

$$C = \frac{d\theta}{d\psi} = -\frac{d\theta}{d\zeta}, \tag{3}$$

and $\theta(\zeta)$ is the soil-water content (see below). The head-based form of the Richards equation has been chosen over the saturation-based version because ζ is continuous and differentiable across the water table and thus can simulate vertical water movement in both the vadose and phreatic zones (Diersch & Perrochet, 1999).

Van Genuchten (1980) describes the use of Mualem theory to characterize the soil properties used in the Richards equation. The soil-water content θ can be expressed in terms of the saturated water content θ_s and the residual water content θ_r. These terms can be combined to give the fractional water content,

$$\Theta \equiv \frac{\theta - \theta_r}{\theta_s - \theta_r} = \frac{\theta - \theta_r}{\Delta\theta}, \tag{4}$$

or $\theta = \theta_r + \Delta\theta\,\Theta$. Mualem theory gives us the following equation describing the relationship between the saturation of the soil Θ and the pressure head term ζ (when $\zeta > 0$)

$$\Theta = (1 + (\alpha\zeta)^n)^{-m}, \tag{5}$$

where $n = \lambda + 1$ and $m = 1 - \frac{1}{n} = \lambda/(\lambda+1)$. α and λ are parameters relating to the soil-water retention properties of the soil.

Using these in equation (3), we find the specific moisture capacity (C) in terms of ζ

$$C(\zeta) = \alpha\lambda\Delta\theta\ \frac{(\alpha\zeta)^{\lambda}\ \Theta}{1 + (\alpha\zeta)^{\lambda+1}}. \tag{6}$$

The expression for the effective hydraulic conductivity in terms of moisture and pressure is given in Van Genuchten (1980)

$$K(\zeta) = K_s\ \Theta^{1/2}\ (1 - (\alpha\zeta)^{\lambda}\ \Theta)^2. \tag{7}$$

When $\zeta \leq 0$, the soil is saturated and then $\Theta = 1$, $C = 0$, and $K = K_s$ (K_s is the saturated hydraulic conductivity). An explanation of the boundary conditions follows (for details of the numerical methods see Appendix A2).

2.1.1. Phreatic Zone and Lower Boundary

At the water table (subscript wt) $z = z_{wt}$, the pressure head is zero ($\psi = 0$) (Pikul et al., 1974). Since $\psi = -\zeta$ we also have $\zeta = 0$ at $z = z_{wt}$. Conditions describing the phreatic zone, namely $C = 0$ and $K = K_s$, hold true for the water table boundary and below, down to an impermeable layer. In this saturated zone, the flux in equation (2), namely

$$F = -K\left(\frac{\partial \zeta}{\partial z} - 1\right), \tag{8}$$

is zero. Since $K = K_s$ in this zone and $\zeta = 0$ at $z = z_{wt}$, it follows that ζ is a simple linear function of z

$$\zeta = z - z_{wt}(t). \tag{9}$$

Note, in general, z_{wt} is a function of time.

When the water table is within the model domain, the lower boundary at $z = 0$ is assumed to be saturated. Using equation (9) for the pressure term in the phreatic zone, the condition at the lower boundary is $\zeta = -z_{wt}$. If the water table is deeper than and below the model domain, then the lower boundary is assigned a zero flux boundary condition. (For numerical implementation see Appendix A2.1.)

2.1.2. Upper Boundary

The top boundary $z = H$ (where H is the depth of the modeled soil domain) is assigned a Neumann (flux) boundary condition defined by precipitation (p_r) and evapotranspiration (e_r) fluxes. This top-flux (F in equation (8) evaluated at $z = H$) is equated to the incoming precipitation minus the surface-moisture-dependent evapotranspiration, $F(H) = p_r - e_r\Theta(H)$. This study assumes grassland vegetation cover with water extraction only at the surface for simplicity.

Daily records of climate variables including precipitation, temperature, wind speed, and relative humidity are required to calculate this top-flux, along with grassland evapotranspiration parameters provided by Dingman (2015). The precipitation can be included directly from total daily records which are resolved over smaller temporal steps by linear interpolation. Atmospherically controlled evapotranspiration is defined by the Penman-Monteith equation, producing a daily average value (see Appendix B).

The influx of water at the surface can never exceed the maximum saturation in the soil. Hence, a further condition has been added to allow ponding at the surface of the domain. Ponding can occur if the soil at the surface is saturated and there is a positive top-flux, $p_r - e_r > 0$. More precisely, ponding occurs if $p_r - e_r > K_s(1 - \partial\zeta/\partial z)$ at $z = H$ where $\Theta = 1$ and thus $\zeta = 0$. To determine if ponding occurs, first the maximum flux, F_m, which the soil can receive is estimated by

$$F_m = K_s\left(1 - \frac{\partial\zeta^*}{\partial z}\right), \tag{10}$$

where $\partial\zeta^*/\partial z$ is calculated using $\zeta = 0$ at $z = H$ and the current value of ζ at the adjacent grid point (see Appendix A2.2). If the incoming flux $p_r - e_r\Theta(H)$ exceeds F_m, then the excess water is stored at the top of the domain as a virtual pond and can be transferred to the top-flux in subsequent time steps when capacity permits. Capacity is made available as water drains or evaporates from the upper regions of the soil. When more water can be infiltrated, the ponded water diminishes. The maximum height of water that can pond above the surface can be altered within HaughFlow to account for different floodplain slopes or surface features affecting surface-ponding capacity—in this paper an estimated levee height is chosen as the maximum ponding depth. (For upper boundary numerical methods see Appendix A2.2.)

2.2. Lateral Flow Component

We use the Boussinesq (1904) equation to simulate lateral hyporheic exchange flow and calculate the position of the water table in the floodplain. The Boussinesq equation is a combination of Darcy's law (1856) for lateral groundwater flow and the continuity equation. It is based on the Dupuit-Forchheimer approximation which states that flow moves horizontally in a shallow groundwater system, driven by the gradient of the water table. The use of this equation for the model setup also simplifies the modeled domain to have a fully penetrating channel at one side and an impermeable horizontal layer below. The equation is presented by Baird and Wilby (1999), with an additional source/sink term

$$\frac{\partial h}{\partial t} = \frac{K_s}{s_y}\frac{\partial}{\partial x}\left(h\,\frac{\partial h}{\partial x}\right) + S(t) - D_r. \tag{11}$$

Here $h(x, t)$ (L) is the height of the water table above the impermeable layer at a given distance x from the river channel at time t. The lateral movement of water from the river is dependent on the saturated hydraulic conductivity, K_s, and the specific yield, s_y. Water is added to or drained from the domain by a source/sink term, $S(t)$, which accounts for water transfer from the vadose zone; this allows for cycles of draining and filling. S varies with time and is determined by calculating the materials balance of the water content in the vadose zone with the applied fluxes at the surface (see Appendix A3.1 for details). D_r is an additional drainage term which accounts for seepage into the underlying stratum and/or groundwater extraction, if negative, and regional groundwater contributions if positive.

2.3. Coupling and Model Spin-up

The interaction between the vadose and phreatic zones is twofold; capillary rise draws water up from the water table, and a source/sink term can account for capillary losses and allow water in the vadose zone to assimilate into the water table. This coupling complexity makes the spin-up calculation a particularly important component of the model. Two options for spin-up can be chosen; one fixes the initial water table and

surface evapotranspiration and runs the simulation over a given number of days, creating a natural gradient of water movement upward from the water table by capillary rise. This, however, does not create natural patterns of water content in the upper regions of the vadose zone which would exist due to a temporal rainfall legacy. For this reason, a more robust spin-up is applied; the code is run over the first year of data as many times as required until the upper regions of soil are consistent with the remainder of the simulation. The latter method, repeated for 2 years, was the chosen spin-up method for this study. Spinning up the model using this method minimizes the influence of the initialization on the model output. (Further details of the initial conditions used are provided in Appendix A3.)

3. HaughFlow Implementation

HaughFlow requires site data, soil parameters, river stage data, and climate data to run. The site data comprises longitude, latitude, elevation, and distance from the river channel. The soil parameters can be subdivided into surface parameters (used for the infiltration component), and lateral, deeper soil parameters (used for the lateral flow component). The van Genuchten parameters used for the infiltration include the saturated and residual water contents, the saturated hydraulic conductivity, and the aforementioned Mualem parameters α and n. For the lateral exchange, another saturated hydraulic conductivity is used, along with a specific yield and the depth to the impermeable layer from the surface. An optional drainage term can be used to account for deep-percolation losses, water table extraction, or regional contributions. The river stage data are input as daily river stage records with an associated zero gauge elevation, for conversion to river water elevation. Finally, the climate data required consist of daily values needed for the evaporation calculation (the mean station pressure, wind speed, maximum and minimum daily temperature, dewpoint temperature, and total precipitation) and for the transpiration calculation (the leaf-area index (LAI), zero-plane displacement, roughness height, top of canopy height, albedo, maximum value of leaf conductance, and a shelter factor).

3.1. Study Site

The Murray-Darling river basin in south-east Australia is one of the largest catchments in Australia (>1 million km^2) (Taylor et al., 2013). We applied HaughFlow to sites adjacent to the Namoi River (drainage area of 40,000 km^2), located in the north-east of the Murray-Darling catchment (Lamontagne et al., 2015) (see Figure 2 for a site map). The climate is subtropical (Lamontagne et al., 2015), characterized by hot, wet summers (December–February), and mild winters (June–August). The vicinity of the study sites has been extensively studied (CSIRO, 2007; Ivkovic et al., 2009; Lamontagne et al., 2011, 2014, 2015; Taylor et al., 2013), providing ample sources for site descriptions, soil properties, and input data sets. A brief description of the sites follows, with the detail required for understanding the model setup. For a more detailed description of the sites see Lamontagne et al. (2015).

The Namoi River at the sites was found to be hydrologically connected to the surrounding floodplain by Lamontagne et al. (2014), meaning exchange with the local water table occurs directly at the channel boundary. This connectivity supports the suitability of applying the laterally hyporheic-driven HaughFlow model. Two locations along the Namoi River, at Old Mollee and Yarral East ~2 km apart, contained three piezometers each, providing time series of water table levels at different distances from the river channel (see Table 1). Piezometer data are monitored by the New South Wales (NSW) Office of Water. The model was applied to evaluate HaughFlow at each of these six sites for time periods of 2.5 and 4 years, depending on data availability.

The input data used to apply the model to this site are summarized in Table 1. CSIRO Division of Soils (Karssies, 2011) provided soil compositions (percentage of sand, silt, and clay from grain size) at different depths for two locations near the study sites, labeled "ed199" and "ed200." The characteristic soil profiles, spanning 2.6 m of depth, were matched with the sites depending on their elevation; "ed199" properties used for lower elevations (<203 m above the Australian Height Datum, AHD) and "ed200" for higher elevations (>203 m AHD). The soil profiles comprised clays, clay loams, and sandy clay loams.

To generate the average van Genuchten parameters, each soil composition was input to the ROSETTA model (Schaap et al., 2001) (for all values see Appendix C). The average of each parameter within the soil

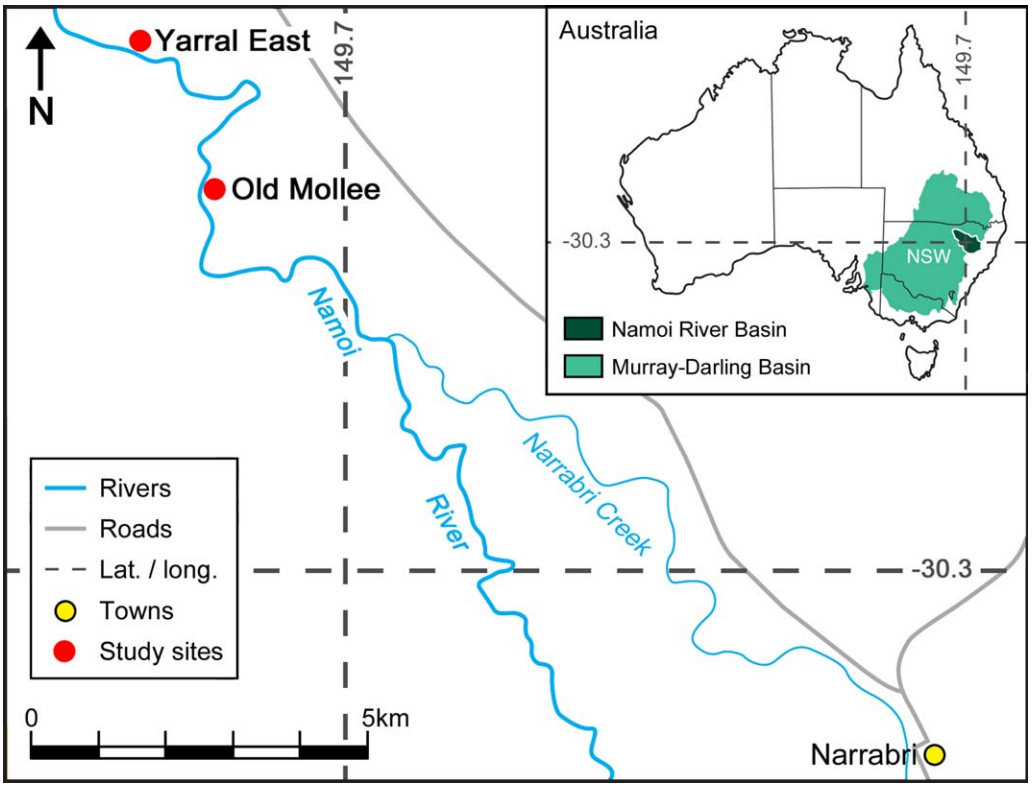

Figure 2. Map (modified from Lamontagne et al., 2015) showing the locations of the study sites along the Namoi river, within the Murray-Darling catchment, in south-east Australia.

profile was used as a simplification of the soil's heterogeneity (Table 2). The van Genuchten properties have a high level of uncertainty attributed to both the range of soil values provided as input as well as to the ROSETTA calculation method. These properties are required for HaughFlow's infiltration component and are expected to differ from the deeper hyporheic soil properties due to anisotropy, and also heterogeneity arising from the prevalence of finer surface sediments from river deposition through channel migration and flooding.

The upper geological layer, the Narrabri Formation, extends to a depth of ~166 m AHD (Lamontagne et al., 2015). A specific yield of 4.5% was calculated for the alluvium by Rassam et al. (2013) using records of stage

Table 1
Summary of the Climate, Soil Profile, River Stage, and Piezometer Data Sets Used for the Study

Data	Reference name	Latitude	Longitude	Elevation (m AHD)
Soil profile	ed199	−30.242	149.664	202
Soil profile	ed200	−30.243	149.694	204
Climate	Narrabri Airport (957340)	−30.317	149.817	230
River stage	Old Mollee (419039)	−30.255	149.680	197.43
River stage	Yarral East (419110)	−30.237	149.671	195.47
Piezometer	Old Mollee (GW098211)	−30.254	149.681	202.25 (50 m to river)
Piezometer	Old Mollee (GW098206)	−30.254	149.682	204.37 (140 m to river)
Piezometer	Old Mollee (GW098207)	−30.254	149.684	203.82 (320 m to river)
Piezometer	Yarral East (GW098208)	−30.237	149.671	202.98 (40 m to river)
Piezometer	Yarral East (GW098209)	−30.236	149.671	202.84 (110 m to river)
Piezometer	Yarral East (GW098210)	−30.234	149.671	202.02 (290 m to river)

Note. The initial data sets were used as model input while the piezometer data were used for comparison with model output. (NB: the elevation column contains values of ground elevation for the climate and piezometer sites and the elevation of the zero gauge for the river stage readings. The piezometer metadata include the distance of each station from the river channel.)

Table 2
*Average van Genuchten Properties for Two Soil Profiles Named "ed199" and "ed200," Calculated Using the ROSETTA Model (*Schaap et al., 2001*)*

Property	ed199 value	ed200 value
θ_r (m^3/m^3)	0.08175	0.09066
θ_s (m^3/m^3)	0.4240	0.4599
α (1/m)	2.171	1.674
n (no units)	1.289	1.300
K_s (m/d)	0.08725	0.1044

heights at nearby Boggabri. The movement of water within this formation was simulated by HaughFlow, with the assumption that the underlying Gunnedah Formation is relatively impermeable with respect to the scale of model simulation. The saturated hydraulic conductivity for the deeper hyporheic component and the drainage term were the most difficult values to measure in the field so they were calibrated using piezometer readings (see section 3.2).

Records of daily meteorological data for sites around the world are provided as part of the Global Summary of the Day (GSOD) (NCDC, NOAA). This source was used to obtain climate records at Narrabri Airport, which is within 17 km from each of the two study locations (Old Mollee and Yarral East). Stream gauges were colocated with these locations, giving daily river stage records corresponding to each site. Model simulations were conducted to evaluate HaughFlow over the common period of piezometer, climate, and stage data for each location; 1 July 2011 to 30 June 2015 for Old Mollee and 1 January 2013 to 30 June 2015 for Yarral East.

The model inputs are plotted in Figure 3; the surface flux at Old Mollee 50 m in Figure 3a, and the river water elevation above the AHD at both locations in Figure 3b. Old Mollee, the upstream location, has water elevations generally >2 m higher than those at Yarral East. The stage data are owned and maintained by the NSW Department of Industry, Skills, and Regional Development (DPI Water).

3.2. Calibration and Sensitivity Analysis

Model calibration was conducted to constrain the two remaining model parameters pertaining to the lateral component of the simulation; the saturated hydraulic conductivity (K_s) and the drainage term (D_r). The two soil parameters control different aspects of the lateral flow signature. K_s controls the fluctuations/variability of the water table levels, so the optimal value was determined by evaluating the water table variability. D_r controls the vertical shift in the mean water table elevation, i.e., it is a vertical permeability or regional infiltration. This variable was calibrated by obtaining the difference between the running average of the modeled and observed values.

The running average ($\overline{Y_i}$) was taken over 31 days, i.e.,

$$\overline{Y_i} = \frac{1}{2m+1} \sum_{j=i-m}^{i+m} Y_i; \quad m=15, \tag{12}$$

for each water table value Y_i. The variability (v) was calculated by taking the difference of each value from the running average, i.e.,

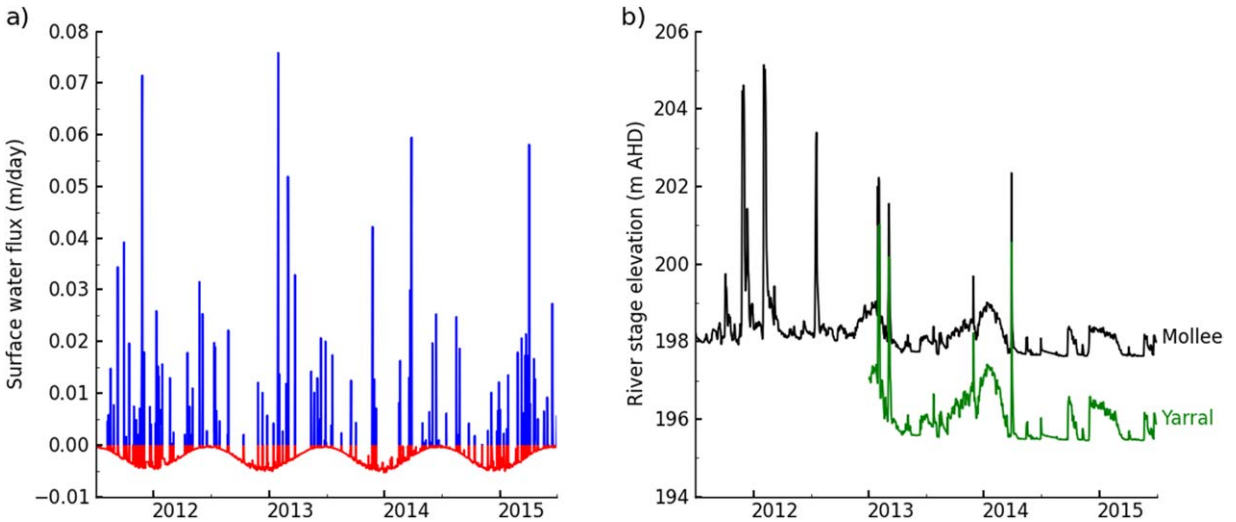

Figure 3. Plots of the surface and lateral inputs to the model. (a) A time series of precipitation minus the actual evapotranspiration at Old Mollee 50 m. (NB: the actual evapotranspiration may vary between sites as it is dependent on the preexisting water at the surface of the soil.) (b) Water surface elevation in the river channel at the two sites along the Namoi River; Old Mollee, and Yarral East (further downstream). AHD stands for the Australian Height Datum.

$$v = \frac{1}{n-2m} \sum_{i=m+1}^{n-m} |Y_i - \overline{Y_i}|, \tag{13}$$

where n is the number of values in the data set. The difference between the observed and modeled variability ($vd = v_{mod} - v_{obs}$) was used to calibrate K_s. The relationship between the two is roughly directly proportional and a result of 0 would be produced by the best fit hydraulic conductivity. The difference in running average (yd) was calculated by

$$yd = \frac{1}{n-2m} \sum_{i=m+1}^{n-m} \left(\overline{Y_{i\,obs}} - \overline{Y_{i\,mod}}\right). \tag{14}$$

The relationship between yd and D_r is also roughly linear and a yd of 0 would be produced by the best fitting D_r.

Full details of the calibration methods and results are provided in Appendix E1. Calibrations were conducted based on two model setups (coupled or uncoupled), two time-frames (2013 or 2014), and at each of the six

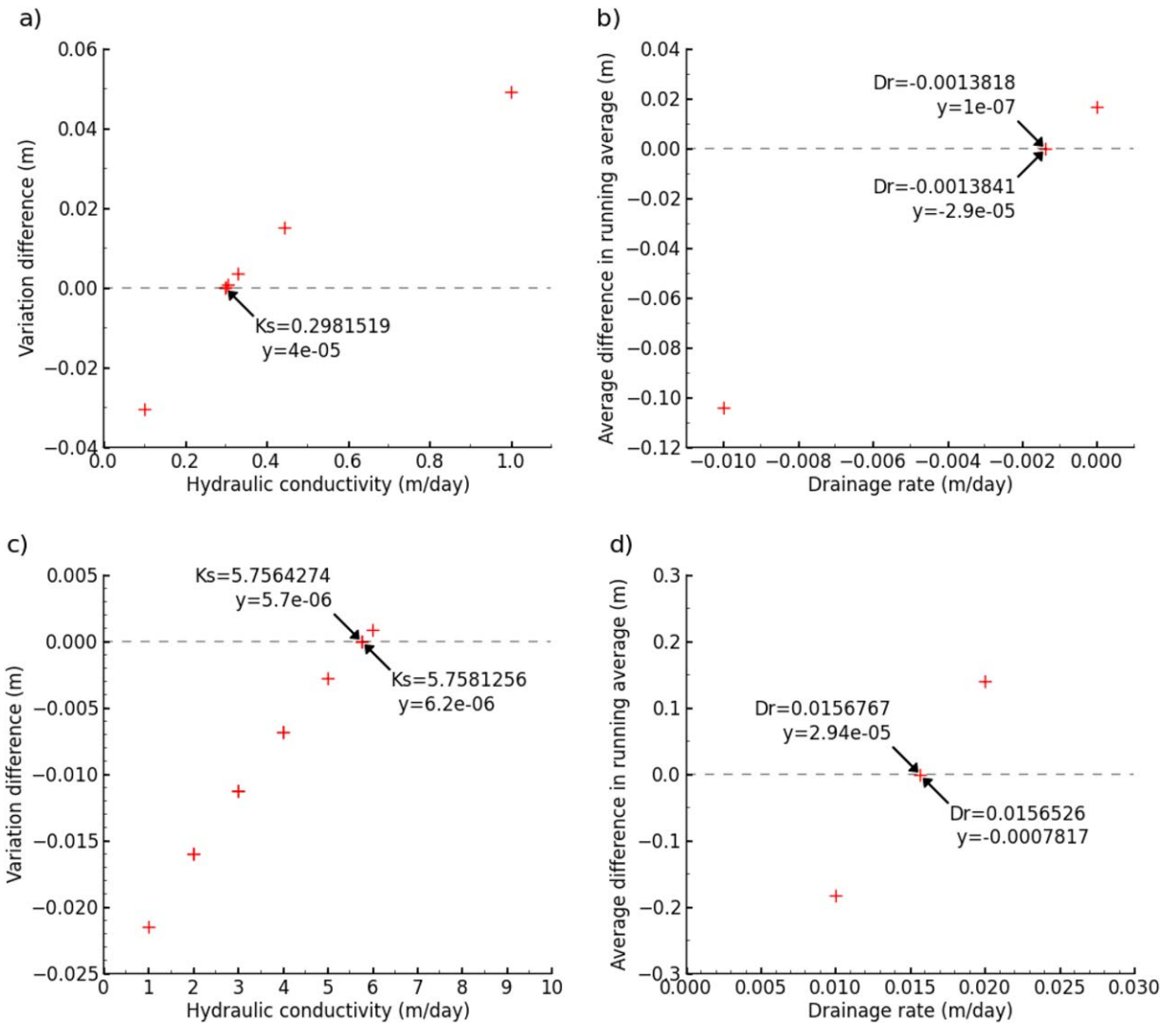

Figure 4. (a and b) Uncoupled 2014 Yarral East 40 m calibration, and (c and d) coupled 2013 Yarral East 290 m calibration. (a and c) The difference in variation between observed and modeled values plotted against the hydraulic conductivity values chosen as input. (A drainage of 0 m/d was used for these simulations.) (b and d) The average difference in running average between observed and modeled values plotted against drainage values. (The hydraulic conductivity calibrated in the associated left-hand plot was used for all drainage calibration simulations.) Simulations did not include vadose zone dynamics.

sites, producing 24 pairs of calibrated parameters. In general, coupled-model calibrations at sites further from the river channel calibrated higher hydraulic conductivities.

The calibration plots for the lowest and highest calibrated hydraulic conductivities are shown in Figure 4. The uncoupled 2014 Yarral East 40 m calibration plots are shown in Figures 4a and 4b, and the coupled 2013 Yarral East 290 m calibration plots are shown in Figures 4c and 4d. Figures 4a and 4c are plots of the water table variability for the iterated range of K_s values, and Figures 4b and 4d are plots of the average differences for the iterated range of drainage values.

The rough linearity between the hydraulic conductivity and the difference in variation, and between the drainage and the average difference in running average, confirms that the dominant effect of these properties on the water table has been captured. High hydraulic conductivity values represent high connectivity with the river channel and lead to high variability in the water table. Conversely, low hydraulic conductivity values smooth the river channel signal in the water table. Positive drainage terms shift the water table values down and vice versa.

Figure 4 also depicts the sensitivity of the model to the lateral flow soil parameters. Looking at the units and values in each of the Figure 4 plots, we can see that the model is much more sensitive to the drainage rate than the hydraulic conductivity. This is because the drainage rate is subtracted directly from the Boussinesq equation (11), while the hydraulic conductivity is tempered by the specific yield and the shape of the water table in the floodplain. The numerical sensitivity is described in Appendix D. Each of the 24 calibrated pairs of parameters were then applied to each of the six sites and evaluation methods were used to determine the most effective calibration configuration (see Appendixes E2 and E3).

3.3. Evaluation Methods

Moriasi et al. (2007) provide guidance for effective model evaluation using statistical tests. Based on these guidelines the model evaluation comprises: a graphical comparison, a standard regression, the Nash-Sutcliffe efficiency (NSE), and the percentage bias (PBIAS).

A standard regression is used to calculate the Pearson's coefficient of determination (R^2), which is a measure of the fit to the linear relationship between the modeled and observed values. A result of 1 is a perfect fit. This classic model evaluation formula is calculated by

$$R^2 = \left(\frac{n\sum Y_{obs}Y_{sim} - \left(\sum Y_{obs}\right)\left(\sum Y_{sim}\right)}{\sqrt{\left[n\sum Y_{obs}^2 - \left(\sum Y_{obs}\right)^2\right]\left[n\sum Y_{sim}^2 - \left(\sum Y_{sim}\right)^2\right]}} \right)^2, \tag{15}$$

where each field-measured value (observed) is given as Y_{obs} and each model-simulated value is Y_{sim}. Each $\sum$ represents the sum over all n values.

The Nash-Sutcliffe efficiency is a ratio of the residual variance (differences between modeled and observed values) to the data variance (spread of the observed values). It is defined by

$$\mathrm{NSE} = 1 - \left[\frac{\sum (Y_{obs} - Y_{sim})^2}{\sum (Y_{obs} - \bar{Y}_{obs})^2} \right]. \tag{16}$$

$\bar{Y}_{obs}$ represents the mean observed value. The resultant NSE values range from $-\infty$ to 1 with values ≥ 0 representing good model-prediction performance (Moriasi et al., 2007). The final test of model performance is percentage bias. This calculates the average tendency of the modeled values to be larger or smaller than their corresponding observed values. The equation for PBIAS is

$$\mathrm{PBIAS} = \frac{100\sum (Y_{obs} - Y_{sim})}{\sum Y_{obs}}. \tag{17}$$

The output is a percentage value, with 0% being optimal. Positive results indicate an underestimation of the values in the model simulation, and negative values an overestimation.

4. Results

The results comprise a model evaluation and a full examination of the model output. The evaluation allows us to determine the level of correlation between the observed and simulated patterns and the output allows us to understand the contribution of each flux within the system to general trends.

4.1. Evaluation

The results of each of the 24 calibrated pairs of parameters and a full discussion of their performance are provided in Appendixes E2 and E3. The results recognize the need to calibrate floodplain models based on the furthest available sites from the river. This is due to the potential to underestimate floodplain connectivity (with low lateral hydraulic conductivity values) at sites nearer the river. Furthermore, the need for fully coupled vadose-phreatic model to fully capture soil-moisture dynamics is exemplified by the distinct improvement in model performance when calibrating based on coupled-model setups. The coupled, 2013, Yarral East 290 m calibration has the best overall performance, with the highest hydraulic conductivity value of any calibration configuration, $K_s = 5.756$ m/d, and a very small drainage term, $D_r = 0.01568$ m. These parameters are used for the simulations throughout the remainder of the study.

Time series of the model and piezometer output are plotted in Figure 5. Model output at all sites for this calibration provides a good general fit to piezometer data. The Old Mollee 320 m site appears to perform worst, followed by the Old Mollee 140 m. At these sites, the highest peaks (i.e., at the beginning of 2012) are underestimated, and gentle rises are overestimated (i.e., at the beginning of 2014). The underestimation of the peaks is discussed further in section 4.2. The overestimation of the gentle rises is because of a higher hydraulic conductivity in the lateral flow component than is required at these sites.

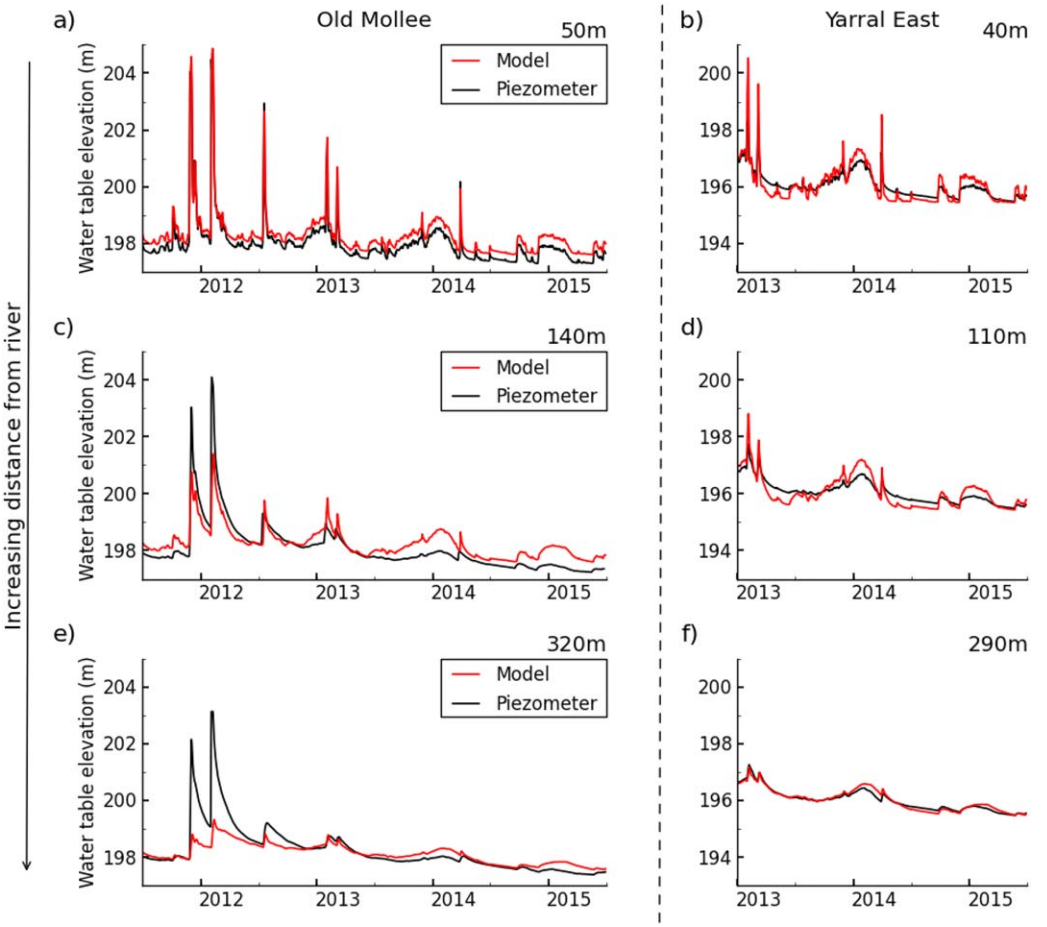

Figure 5. Model and piezometer output for all the sites, including the Yarral 320 m site (bottom left) of which the year 2013 was used for the calibration.

Table 3
Results of the Statistical Tests Carried out on the Simulated Model Output Data Compared With the Observed Field-Measured Data

Data	R^2	NSE	PBIAS	Days
Old Mollee 50 m	0.974	0.855	−0.145%	1,462
Old Mollee 140 m	0.817	0.694	−0.093%	1,456
Old Mollee 320 m	0.735	0.520	−0.063%	1,461
Yarral East 40 m	0.849	0.575	−0.005%	912
Yarral East 110 m	0.811	0.566	−0.002%	912
Yarral East 290 m	0.946	0.939	−0.002%	912
Best/worst values	1/0	$1/-\infty$	$0/\infty$	

Note. The Pearson's R^2, Nash-Sutcliffe Efficiency, percentage bias, and number of days used in the calibration are provided for each of the sites.

The model outputs appear to provide a generally good representation of water dynamics, but the evaluation parameters can help us quantify the extent of the fit. The detailed evaluation results chosen calibration are listed in Table 3. Overall, the results are very good. The Pearson's R^2 values, which are a measure of the linear fit between the model and piezometer data sets, are all >0.7 (with a value of 1 representing a perfect fit). The NSE is a ratio of the residual to the data variance (a value of 1 indicates equal variability in each), hence if the variability of the model output is within the scope of the piezometer variability then the NSE value shows good model performance. Hence, Old Mollee 320 m, with visibly less variability in model than piezometer data, has the poorest NSE value. Nevertheless, all NSE values were >0.5.

The PBIAS values are a measure of the offset of the model data to the piezometer data. The results are all slightly negative, indicating an overestimation of model values, with the best results (closest to 0%) at the sites furthest from the channel and becoming poorer closer to the river. The Yarral East 110 and 290 m sites (Figures 5d and 5f) have the smallest PBIAS values. This can be attributed to the model values being slightly above or slightly below piezometer readings in roughly equal measures, hence the offset (drainage term) is optimal at these sites. The modulus of the PBIAS values at all sites were $<0.15\%$. Overall, as expected, the Yarral East 290 m site performs best. The perceived worst performer in the visual comparison (Old Mollee 320 m) is substantiated by the results in Table 3.

4.2. Model Output

Time series of soil saturation Θ within a vertical slice of the floodplain, three distances from the river channel, and across two different locations are exhibited in Figure 6. To understand the contribution of each flux (i.e., precipitation and lateral flow) to the soil, we can study soil-water patterns related to the following three categories: the phreatic zone ($\Theta = 1$), the vadose zone ($\Theta < 1$), and interactions between the two zones. In the phreatic zone, the most apparent trend is that of reduced variability in the water table with distance from the river channel. In hydraulically connected floodplains, the water table is driven by river stage fluctuations that propagate and dissipate through the floodplain. Hence, the water table is less connected to the river channel with distance, making it less sensitive to changes in river water elevation and having the effect of smoothing the phreatic signal to remove extremes. Along with a dampening of the water table signal, there is a time delay, on the order of weeks. Peaks and troughs observed closer to the channel take time to propagate to the further sites, so rising and falling limbs are more gradual in the time series. There is also a very gradual decrease in average water table levels in the model output due to the positive drainage term.

Soil-moisture patterns in the upper part of the vadose zone are dominated by the surface flux. The climate inputs were the same for all six sites, so saturation patterns in the upper part are consistent. Soil saturation near the surface fluctuates, as heavy rains and evapotranspiration lead to saturated and dry soil-moisture extremes, respectively. The temporal legacy of individual rainfall events is exhibited in the angle of its infiltration front as it progresses downward (see labeled infiltration on Figure 6e). Moving deeper into the soil, moisture fluctuations dampen and base soil saturation gradually increases. The increase in saturation is a result of slow infiltration rates, accumulating rainfall contributions, and the influence of the capillary fringe.

The capillary fringe below contributes soil-moisture to a significant depth interval of the vadose zone. The extent of this depth is influenced by the soil properties. This contribution is more visible at the near-stream sites (Figure 6a Mollee 50 m and Figure 6b Yarral 40 m), where capillary contributions from a higher water table interact more readily with the soil-moisture extremes from rainfall events. The capillary fringe moisture contribution is also more prominent at the further upstream Old Mollee sites, which have water table values at higher elevations and hence higher capillary fringes, than at Yarral East sites. It must be noted, however, that the floodplain surface elevation varies across the sites, which also affects the location of the water table with respect to the soil surface.

At Old Mollee 50 m (Figure 6a) in early and mid-2012, the moisture in the capillary fringe connects with the infiltrating precipitation creating a region of very high saturation that reaches the surface. This underground connectivity, combined with high variability in water table levels, leads to a higher risk of flooding near the

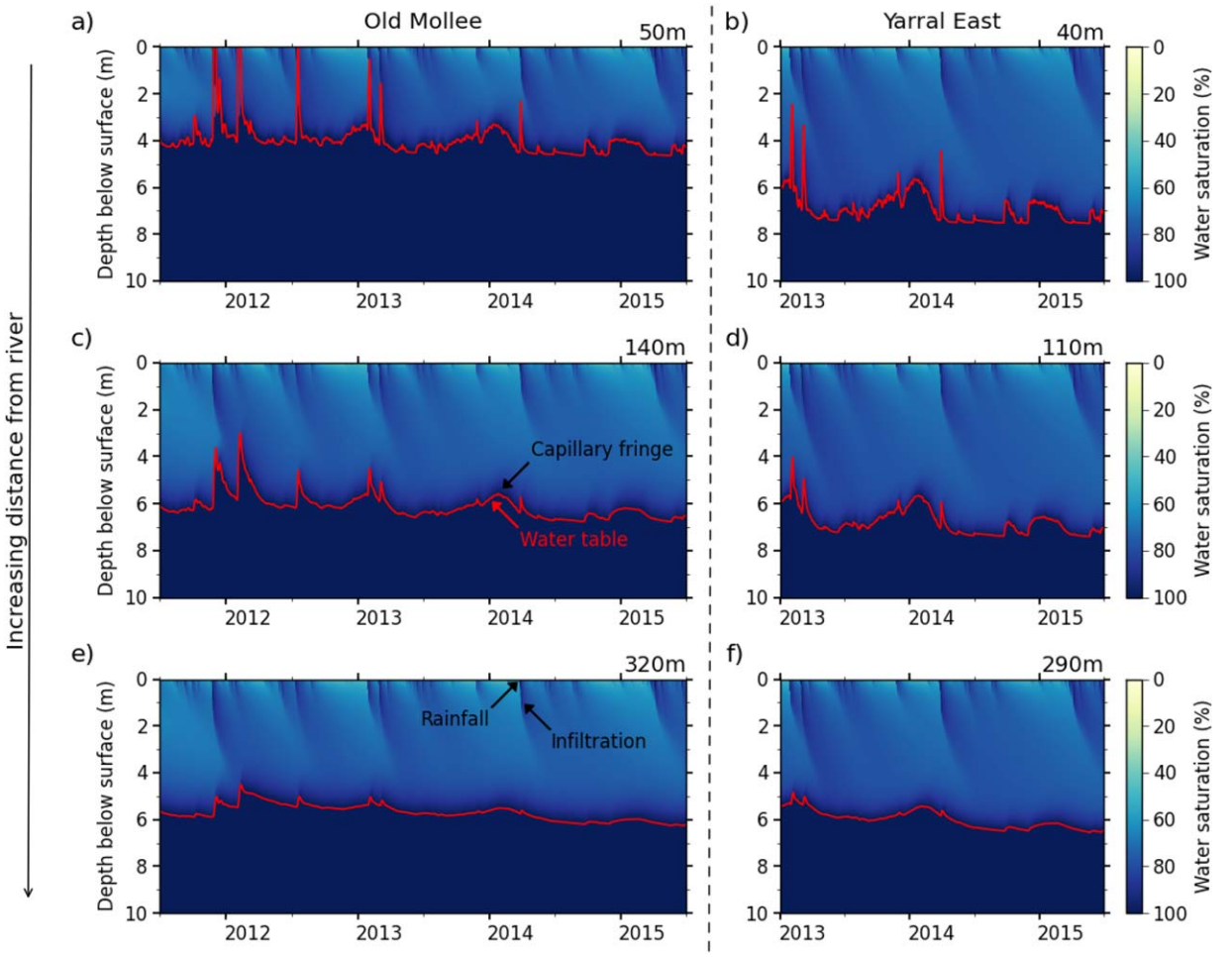

Figure 6. Saturation plots showing the upper 10 m of soil across the time series of sites at Old Mollee (left column), (a) 50, (c) 140, and (e) 320 m from the river channel, and at Yarral East (right column), (b) 40, (d) 110, and (f) 290 m from the river channel. The elevation of the land at each site is (a) 202.25, (c) 204.37, (e) 203.82 m above the Australian Height Datum (AHD) (left column), and (b) 202.98, (d) 202.84, and (f) 202.02 m AHD (right column).

river channel—irrespective of overbank conditions. Spikes in the water table due to capillary fringe connection with infiltrating water also occur in early 2013 and 2014 but do not rise as far as the soil surface. Using this knowledge of increased connectivity in the vadose zone when the capillary fringe meets infiltrating water, we can look back at the model and piezometer comparisons (Figure 5), specifically at Mollee 140 m (c) and Mollee 320 m (e), and see that the under-prediction of water table peaks in early 2012 may be due to inaccuracies in the bulk soil properties used in the infiltration calculation (equation (2)). A higher saturated hydraulic conductivity in the vadose zone, for example, would lead to faster infiltration of rainfall events allowing them to connect with associated peaks in the capillary fringe. This exemplifies the importance of the relationship between the vadose and phreatic zones for understanding patterns of water change in each.

4.3. Decadal Simulation

Applying HaughFlow to a decadal time series allows us to investigate the response of soil-moisture distributions to climatic fluctuations. Climate data from the Inverell Research Centre (station ID 94541099999, GSOD) provided a decadal time frame for the inputs. The Inverell Research Centre is located at −29.78, 151.08 and has continuous data available from the beginning of 2003. Figure 7 shows the results of the longer input series at the Old Mollee 140 m site from 2004 to 2017. Comparing the surface flux (Figure 7a) and river stage (Figure 7c) inputs with the soil saturation output (Figure 7b) allows us to fully examine the soil-moisture profiles and how each process drives changes. During the Australian summer months (December–February), patterns of heavy rainfall and strong evaporative drying are seen in Figure 7a, and replicated in

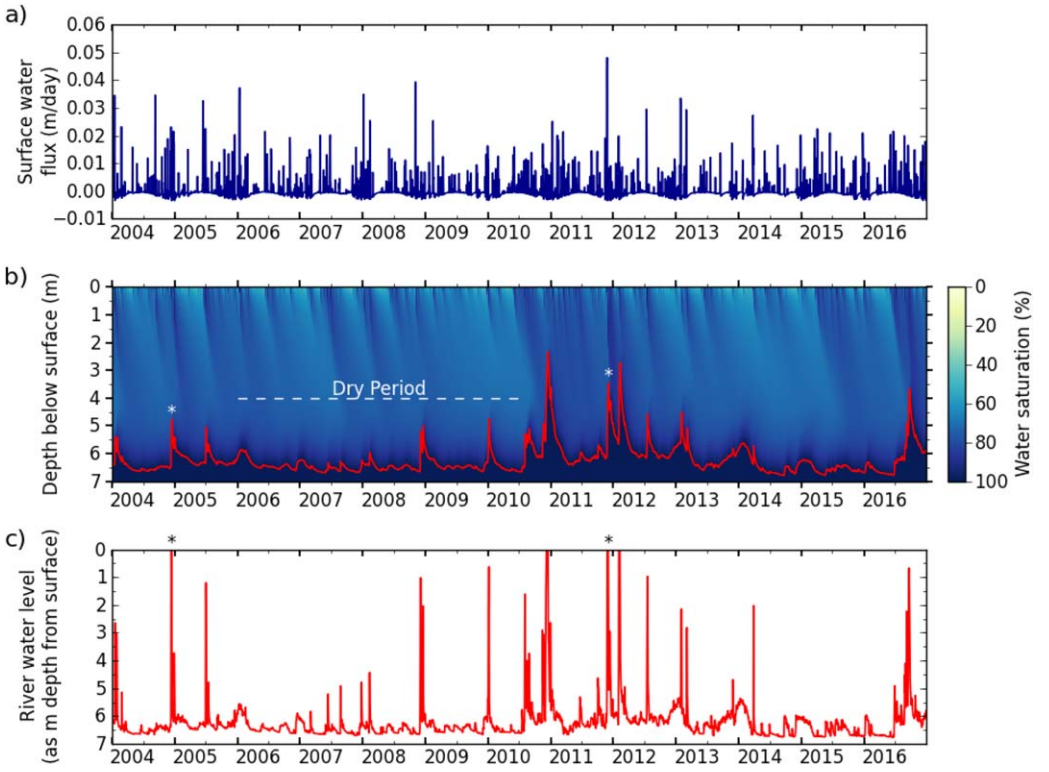

Figure 7. (a) Plots showing the surface flux, (b) saturation profile, and (c) river stage time series for Old Mollee 140 m from 2004 to 2017. A particularly dry period in the soil is annotated with a white dashed line, and asterisks mark two similar peaks in the river stage and water table plots

Figure 7b where they diffuse diagonally downward in time within the soil. River stage variations in Figure 7c are replicated in the water table (Figure 7b) with a time delay of approximately 24 days (which emerges directly from the Boussinesq equation, 140 m/K_s), and a reduced amplitude.

Comparing similar river stage peaks in late 2004 and late 2011 (asterisks in Figures 7b and 7c), the second peak is much more pronounced in the water table than the first. The only difference between the two being that soil-moisture levels were much higher deep in the soil preceding the second peak. Hence, river stage peaks are more pronounced in the water table when preceded by rainfall events that have infiltrated deep into the soil. There is a visible period of dryness in the soil, particularly for midrange depths from 2006 to mid-2010 (white dashed line in Figure 7b). Looking at Figure 7c, this dryness seems to be triggered by low river stage values from late 2005 to late 2008. Low rainfall in 2009 exacerbates this drying. This dry period matches the time frame of the southeast Australian "Millenium" drought (2001–2009), during which time groundwater storage was found to be particularly depleted from the end of 2006 until the beginning of 2010 (Van Dijk et al., 2013). Soil-moisture throughout the soil recovered in 2011 and 2012, which were very wet years due to a combination of high rainfall events and high river stage peaks.

The power of this model is its ability to quantify the water availability to rooting vegetation, in particular within dynamic and sensitive riparian environments, at different distances from the river. Plant species, depending on their rooting depths, may access different potential water reservoirs in the floodplain. To compare water availability for different plants at different locations, time series of water content was produced over depth intervals. The soil-moisture was rescaled from saturation Θ (values range from 0 to 1), to a raw value of actual water content θ within a meter of soil (values range from the residual water content θ_r, to the saturated water content θ_s). Using the water content allows us to quantify the actual water available to vegetation rather than merely how filled the pore spaces are. In Figure 8, (a) Old Mollee 50 m, (b) Old Mollee 140 m, and (c) Old Mollee 320 m are compared. The plots show the water content in 1 m intervals down to 5 m. The saturated and residual water content for a 1 m depth range are provided as references for each plot.

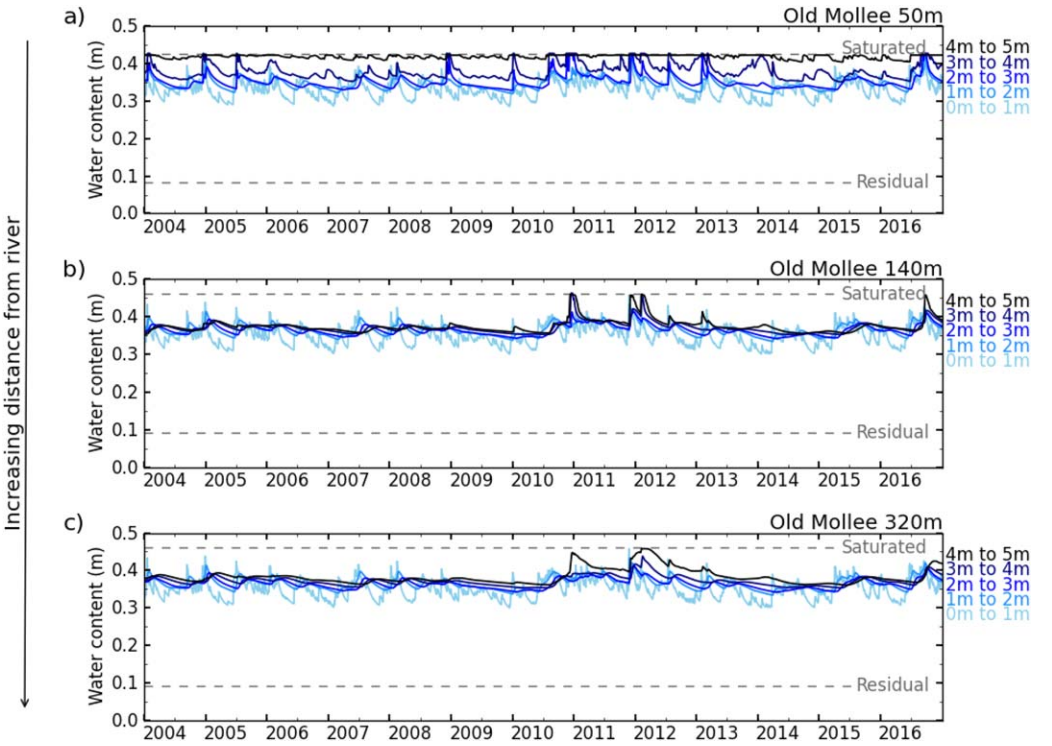

Figure 8. The water content in 1 m depth intervals (θ) down to 5 m for (a) Old Mollee 50 m, (b) Old Mollee 140 m, and (c) Old Mollee 320 m. The shades of blue in the plot become darker with depth into the soil.

The uppermost depth interval (0–1 m) at all the sites has the highest variability and contains the lowest overall levels of daily water content. Deeper-rooting vegetation has access to more water overall. The "0 m to 1 m" depth range is almost identical among all the three sites, yet differences become more pronounced moving deeper into the soil. The water content across all depths is high at Old Mollee 50 m, with near-complete saturation maintained within the 4–5 m depth. Saturation in this depth range indicates that the water table has risen to 4 m depth. The dry period identified between 2006 and mid-2010 in Figure 7 can be seen more clearly in the Old Mollee 140 and 320 m plots (Figures 8b and 8c). This is because the baseline water table depth is below 5 m for Old Mollee 140 and 320 m (see Figures 6 and 7b). So these depths are meters away from both the soil surface and the water table, making them more sensitive to periods of drought. When we compare the peaks in the 4–5 m water content in late 2010, late 2011, and early 2011 they decline more gradually in sites furthest from the river. This is because the water table further from the river is less variable. As water table levels are maintained for longer, the capillary fringe prolongs the decline to baseline water content levels. At the Old Mollee 320 m site, the capillary fringe allows water to be retained for up to months at 4–5 m deep. Hence, the water content just above the water table, further from the river is actually a much more reliable supply than above the water table nearer the river, which is more prone to daily fluctuation.

To further investigate the influence of the capillary fringe, we can observe the sharp difference in water content in the peaks between 3–4 and 4–5 m depths in Figure 8c, indicating the extent of the capillary fringe. Hence, the draw from the capillary fringe is not indefinite. Conversely, changes in water content moving down from the surface are more gradual, since water can continue infiltrating over time. Figure 9 allows us to examine these moisture patterns in a different way. Each column in the figure represents one of the Old Mollee sites, with histograms to the right representing sites further from the river.

The shape of the histograms indicates the mean and variance in water availability for each depth interval. Bell-shaped curves (i.e., all three 0–1 m histograms: Figures 9a–9c) represent depths that are sometimes exposed to extremes of wet and dry water conditions. Right-skewed distributions (i.e., the 2–3 m soil depth at Old Mollee 50 m and the 4–5 m depth at Old Mollee 320 m: Figures 9g and 9o) have a consistent lower

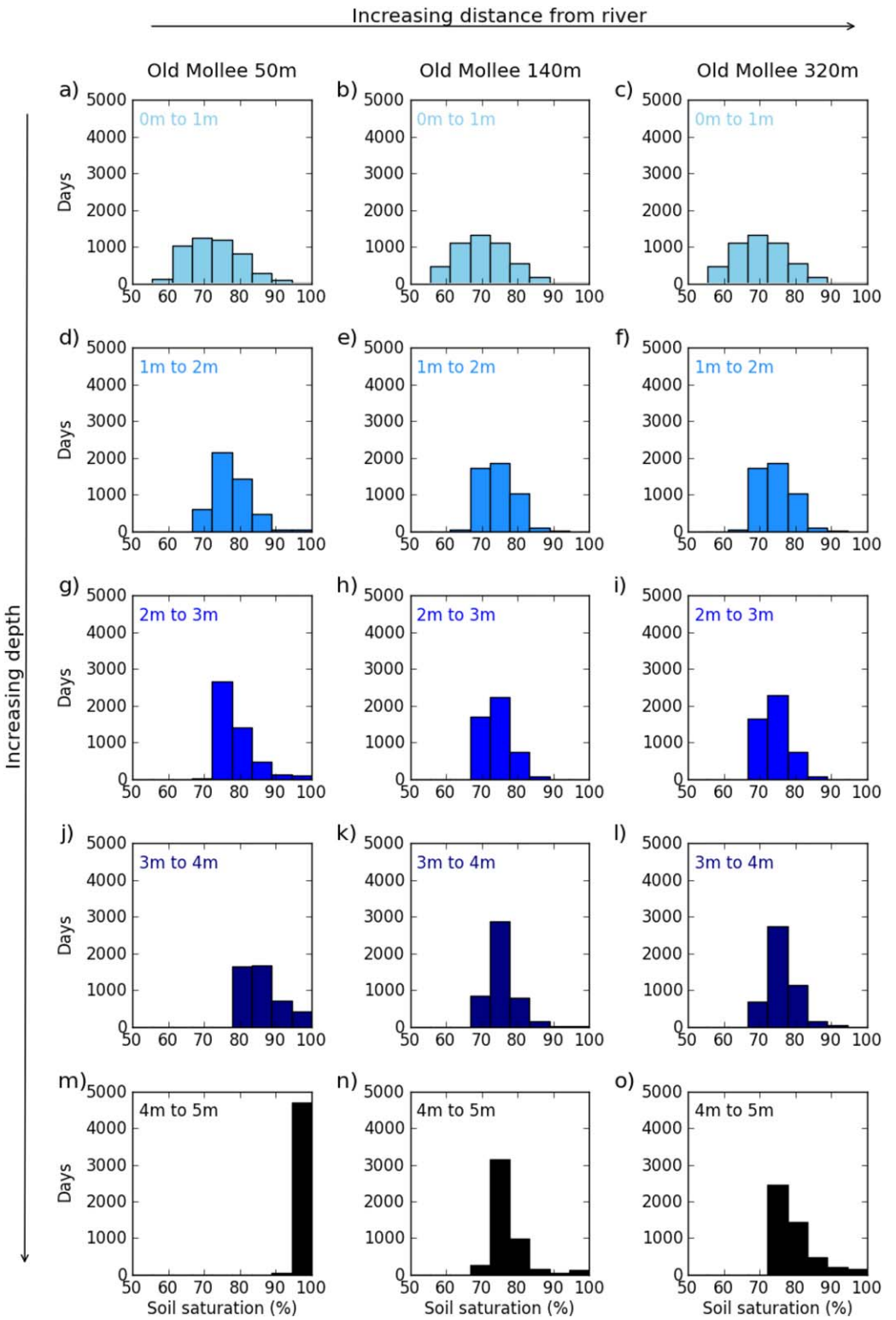

Figure 9. Histograms of the soil saturation in 1 m depth intervals (up to 5 m) for (the first column: a, d, g, j, and m) Old Mollee 50 m, (the second column: b, e, h, k, and n) Old Mollee 140 m, and (the third column: c, f, i, l, and o) Old Mollee 320 m. Plots further down in the figure represent soil saturation deeper in the soil.

threshold of water availability. The left-skewed distribution in Figure 9m portrays a depth with both high and consistent water availability. The highest water contents (all >70%) are located at 2–3, 3–4, and 4–5 m at the Old Mollee 50 m site and at 4–5 m at the Old Mollee 320 m site. The higher content at the Old Mollee 50 m site is because the water table is higher at this site (at ∼4 m). The higher content at the deepest Old Mollee 320 m site is because of the low variability in the water table located a few meters below (at ∼7 m deep). Hence, the water availability is higher and more reliable nearer the water table and further from the river channel. Depending on the water requirements and rooting depths of a particular plant species, plots like these could be used to analyze current, or plan future riparian plantations. Furthermore, climate projections can be used to create these plots for future scenarios to investigate the water balance, soil-moisture, and vegetative water availability for a range of scientific and management applications.

5. Discussion

In this paper, we developed a new model with the capability to analyze coupled soil-moisture and water table fluctuations. Our model, HaughFlow, enables simple simulation of subsurface water fluxes in floodplains, through dynamic coupling of lateral hyporheic flow and rainfall infiltration, based on existing theoretical frameworks. We have coded this model in a manner that enables straightforward calibration of water table fluctuations and allows for decadal simulations of the impact of climate or even climate change on subsurface moisture. Water availability in catchments like the Murray-Darling basin are under increasing pressure from agricultural production and human use (Pittock & Connell, 2010). Having already experienced prolonged periods of drought, the majority of climate change scenarios foresee further water scarcity in the Murray-Darling region (Pittock & Connell, 2010). HaughFlow could be used to assess the impacts to water availability at multiple depths, and help inform water and ecological management plans.

Our application of HaughFlow to sites in southeast Australia identified a best approach for model calibration. The model performed best when calibrated using piezometer sites furthest from the river. This is due to the propensity for otherwise underestimating floodplain connectivity with a low lateral hydraulic conductivity value. We also showed the utility of the coupled-model approach, which significantly improves model performance. Further work is necessary to calibrate the unsaturated model component using high resolution data on soil-moisture.

The model outputs demonstrate the importance of the interdependence of the vadose and phreatic zones. In the upward direction, the capillary fringe contributes to soil-moisture patterns and connectivity in the vadose zone; and downward, the temporal legacy of infiltrating water in the vadose zone manifests as increased water content stored deeper in the soil. High antecedent moisture conditions in the vadose zone can facilitate connection between rising and infiltrating waters, raising the water table. Hence, the capillary fringe is an important exchange pathway between the vadose and phreatic zones. The vadose zone provides a significant store of water, particularly within the capillary fringe, which replicates fluctuations in the water table, and retains high levels of water saturation after peaks in the water table. This provides a critical moisture resource for shallow-rooting plants that are unable to reach the water table, which is particularly important further from the river channel.

Water table fluctuations became more delayed and less variable with distance from the river. At the furthest sites, delays in the propagation of river stage peaks are on the order of weeks, and the reduced variability means storage in the capillary fringe can maintain high water content for up to months. This storage potentially provides a valuable water resource to deeply rooting plants, particularly later in the dry season.

Differences between depths in the vadose zone were explored further using decadal data sets. Seasonal patterns in the surface flux were clearly visible in the upper regions of soil, i.e., the high rainfall and strong evapotranspiration rates during the summer months. As a result of the "Millenium" drought (Van Dijk et al., 2013), an extended dry period was observed in the soil, and its causes easily identified by comparison with the two input data sets (Figure 7). Critical depths and locations in the floodplain that were most sensitive to this dry period were also determined. Changes in soil-moisture patterns are more gradual with movement down from the soil surface as water infiltrates continuously. Conversely, with movement up from the water table there is a jump down in water content, as the extent of the capillary fringe is reached (seen in Figure 8). Overall, higher and more consistent water contents occurred in the soil regions that were both closer to the water table and further from the river channel.

Water content over different depth ranges allow HaughFlow to be used for a range of scientific and management applications relating to water and vegetation. If the rooting depths are known for a particular riparian species, then knowledge of the soil-water saturation over that depth can elucidate changes in the plant's behavior. Of course, root-water uptake is not as simple as this, as is it challenging to accurately represent root-water uptake with depth (Feddes et al., 2001) and plants can grow to adapt to their water availability (Canham et al., 2012). For example, river red gum trees in the Murray-Darling Basin were found to adapt well to the "Millenium" drought (Doody et al., 2015). So for most effective results, HaughFlow should be used alongside knowledge of plant physiology.

The combination of different processes working in tandem within the riparian vadose and phreatic zones make floodplains highly dynamic in terms of hydrology and water availability to vegetation. To better understand the relative contributions of each process, further work could be done to decouple their interlocking signals within the floodplain. One such way would be by delineating the capillary fringe. This is hard to do precisely, due to dynamic baseline soil-moisture conditions, no clear moisture threshold for the fringe, and unknown contributions from water infiltration. The incorporation of stable isotope tracers in HaughFlow could be used to establish water sourcing (Gat, 1996; Kendall & McDonnell, 2012). This would also make the model more powerful for use in vegetative water-use analysis, as plants take-up and store the stable isotopes from water at their rooting depths (Ehleringer & Dawson, 1992).

Appendix A: Numerical Methods

The numerical methods for the Richards equation and the Boussinesq equation are explained in the following subsections. A schematic of the physical and computational domains is shown in Figure A1.

The lateral domain extends from the river channel ($x = W$, grid point $i = n_x$) to the internal floodplain ($x = 0$, grid point $i = 0$). The computational grid points in the vertical domain are located at midlayers. Across both systems the vertical domain begins at the impermeable layer ($z = 0$, grid point $i = -1/2$) up to the soil surface ($z = H$, grid point $i = n_z + 1/2$). Richards equation can be applied to any position along the lateral domain; in Figure A1 this is displayed as the midpoint on the lateral axis for simplicity. The spatial steps are $\Delta x = W/n_x$ and $\Delta z = H/n_z$.

The boundary conditions in the model consist of:

1. A prescribed flux (defined by the precipitation and surface evapotranspiration) at $z = H$ in the Richards equation.

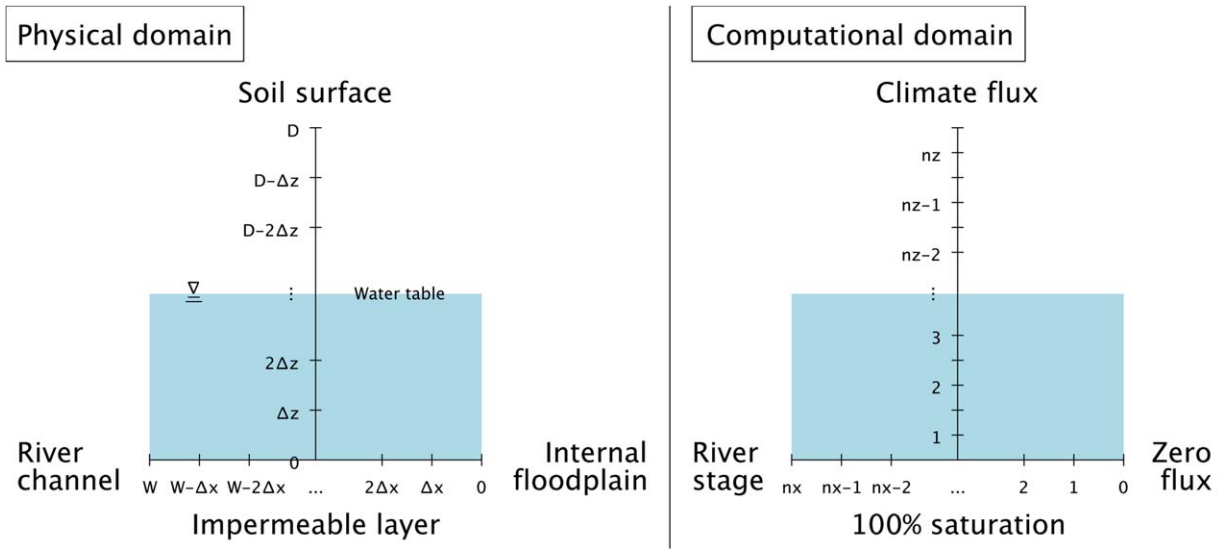

Figure A1. Physical and computational domains used in the Richards equation (vertical) and in the Boussinesq equation (horizontal). NB: if there is no water table/phreatic zone in the modeled domain, the bottom boundary becomes a zero flux condition.

2. A specified hydraulic head ($\psi = -\zeta = z_{wt}$) at the impermeable lower boundary $z = 0$ in the Richards equation, or a zero flux condition if there is no water table within the modeled domain.
3. A prescribed river water elevation at $x = W$ in the Boussinesq equation.
4. A zero flux condition at the far-channel extent of the Boussinesq equation.

The two equations are coupled through the water table. Specifically, the water table height $z_{wt}(t)$ provides the lower boundary condition in the Richards equation, while the flux at the water table boundary arising from the vadose zone provides the source term S in the Boussinesq equation. Details are given below.

A1. Initialization

The initialization of the water content throughout the vadose and phreatic zones is described herein. In equilibrium, with a constant level of water h_r in the river channel, and no external influences (including no surface flux), the water table will eventually equilibrate laterally with the adjacent floodplain. This means the water level will become uniform throughout ($h(x,0) = h_r$) and there will be no vertical flux. Hence, the zero flux solution $\zeta(z,0) = z - z_{wt}$ in equation (9), with $z_{wt} = h_r$ can be applied throughout the domain.

A2. Richards Equation

Vertical water movement is simulated using the Richards equation (equation (2)) along with three equations for Θ (5), C (6), and K (7). For numerical simplicity, the following substitutions are applied to the three equations when $\zeta > 0$

$$\begin{aligned} C_s &= \alpha\lambda\Delta\theta \\ \tau &= (\alpha\zeta)^{\lambda} \\ \xi &= (1+\alpha\zeta\tau)^{-1}. \end{aligned} \tag{A1}$$

These lead to the following equivalent forms of equations (5)–(7)

$$\begin{aligned} \Theta &= \xi^m \\ C(\zeta) &= C_s\tau\Theta\xi \\ K(\zeta) &= K_s\Theta^{1/2}(1-\tau\Theta)^2. \end{aligned} \tag{A2}$$

When $\zeta \leq 0$, the soil is saturated; there these functions simplify to the constants $\Theta = 1$, $C = 0$, and $K = K_s$. These constants apply to the grid points below the water table.

Following Pikul et al. (1974), a tridiagonal formula along with a predictor-corrector scheme was used to evolve equation (2) in time. The main difference from Pikul et al. (1974) is in placing grid points at midlayer depths, as this simplifies the upper boundary condition. We also use ζ in place of ψ.

The predictor step from $t = n\Delta t$ to $(n+1/2)\Delta t$ at each interior vertical grid point, $i = 2,\ldots, n_z - 1$, for equation (2) uses the following discretization:

$$C_i^n \frac{\zeta_i^{n+1/2} - \zeta_i^n}{(\Delta t/2)} = \frac{K_{i+1/2}^n}{\Delta z}\left(\frac{\zeta_{i+1}^{n+1/2} - \zeta_i^{n+1/2}}{\Delta z} - 1\right) - \frac{K_{i-1/2}^n}{\Delta z}\left(\frac{\zeta_i^{n+1/2} - \zeta_{i-1}^{n+1/2}}{\Delta z} - 1\right), \tag{A3}$$

where the grid-averaged conductivity term is defined by $K_{i+1/2} = \frac{1}{2}(K_i + K_{i+1})$. Using the constants

$$\sigma_1 = \frac{\Delta t}{2\Delta z} \quad \& \quad \sigma_2 = \frac{\Delta t}{2\Delta z^2}, \tag{A4}$$

we can rearrange this equation into tridiagonal form:

$$\begin{aligned} &-\sigma_2 K_{i+1/2}^n \zeta_{i+1}^{n+1/2} + \left(C_i^n + \sigma_2 K_{i+1/2}^n + \sigma_2 K_{i-1/2}^n\right)\zeta_i^{n+1/2} - \sigma_2 K_{i-1/2}^n \zeta_{i-1}^{n+1/2} \\ &= \sigma_1\left(K_{i-1/2}^n - K_{i+1/2}^n\right) + C_i^n \zeta_i^n. \end{aligned} \tag{A5}$$

With the solution for $\zeta_i^{n+1/2}$, we can use equations (6) and (7) to obtain values for $K_i^{n+1/2}$ and $C_i^{n+1/2}$ for $i = 1,\ldots, n_z$. From $K_i^{n+1/2}$, we obtain $K_{i+1/2}^{n+1/2} = (K_i^{n+1/2} + K_{i+1}^{n+1/2})/2$ as before. Using $\Theta_{n_z}^{n+1/2}$, we can then update the flux term $F^{n+1/2}$. The corrector step from $t = n\Delta t$ to $(n+1)\Delta t$ for the Richards equation is then calculated from

$$C_i^{n+1/2}\frac{\zeta_i^{n+1}-\zeta_i^n}{\Delta t}=\frac{K_{i+1/2}^{n+1/2}}{2\Delta z}\left(\frac{\zeta_{i+1}^{n+1}-\zeta_i^{n+1}}{\Delta z}-1\right)-\frac{K_{i-1/2}^{n+1/2}}{2\Delta z}\left(\frac{\zeta_i^{n+1}-\zeta_{i-1}^{n+1}}{\Delta z}-1\right)+\frac{K_{i+1/2}^{n}}{2\Delta z}\left(\frac{\zeta_{i+1}^{n}-\zeta_i^{n}}{\Delta z}-1\right)-\frac{K_{i-1/2}^{n}}{2\Delta z}\left(\frac{\zeta_i^{n}-\zeta_{i-1}^{n}}{\Delta z}-1\right), \tag{A6}$$

which we can rearrange as

$$-\sigma_2 K_{i+1/2}^{n+1/2}\zeta_{i+1}^{n+1}+\left(C_i^{n+1/2}+\sigma_2 K_{i+1/2}^{n+1/2}+\sigma_2 K_{i-1/2}^{n+1/2}\right)\zeta_i^{n+1}-\sigma_2 K_{i-1/2}^{n+1/2}\zeta_{i-1}^{n+1}=C_i^{n+1/2}\zeta_i^n+\sigma_1\left(K_{i-1/2}^{n+1/2}-K_{i+1/2}^{n+1/2}+K_{i+1/2}^{n}\left(\frac{\zeta_{i+1}^{n}-\zeta_i^{n}}{\Delta z}-1\right)-K_{i-1/2}^{n}\left(\frac{\zeta_i^{n}-\zeta_{i-1}^{n}}{\Delta z}-1\right)\right). \tag{A7}$$

When the water table is above the highest grid point in the domain, then flooding occurs. For flooding, no infiltration calculation is required and the surface flux is assigned at the water table boundary, $F_{wt}=p_r-e_r$. Evaporative fluxes can then diminish the water through the sink term in the lateral flow calculation until a vadose zone is formed (see Appendix A3.1 for more details on the calculation of the sink term).

A2.1. Lower Boundary

At the lowest grid point, $i=1$, we make use of the bottom boundary condition $\zeta=-z_{wt}$. Taking ζ to be a linear function of z near $z=0$ then leads to $\zeta_0=-2z_{wt}-\zeta_1$. This results in the following predictor and corrector equations:

$$-\sigma_2 K_{3/2}^{n}\zeta_2^{n+1/2}+\left(C_1^n+\sigma_2 K_{3/2}^n+2\sigma_2 K_{1/2}^n\right)\zeta_1^{n+1/2}=\sigma_1\left(K_{1/2}^n-K_{3/2}^n\right)+C_1^n\zeta_1^n-2\sigma_2\Delta z K_{1/2}^n z_{wt}, \tag{A8}$$

and

$$-\sigma_2 K_{3/2}^{n+1/2}\zeta_2^{n+1}+\left(C_1^{n+1/2}+\sigma_2 K_{3/2}^{n+1/2}+2\sigma_2 K_{1/2}^{n+1/2}\right)\zeta_1^{n+1}=\sigma_1\left(K_{1/2}^{n+1/2}-K_{3/2}^{n+1/2}+K_{3/2}^n\left(\frac{\zeta_2^n-\zeta_1^n}{\Delta z}-1\right)-K_{1/2}^n\left(\frac{2\left(\zeta_1^n-z_{wt}\right)}{\Delta z}-1\right)\right)+C_1^n\zeta_1^n-2\sigma_2 K_{1/2}^{n+1/2}z_{wt}. \tag{A9}$$

When the water table is below the lowest half-grid point ($z_{wt}<\Delta z/2$), the domain is considered to be unsaturated everywhere. In this case, a zero flux condition is applied at $z=0$. For this case, the predictor step is

$$-\sigma_2 K_{3/2}^n\zeta_2^{n+1/2}+\left(C_1^n+\sigma_2 K_{3/2}^n\right)\zeta_1^{n+1/2}=C_1^n\zeta_1^n-\sigma_1 K_{3/2}^n, \tag{A10}$$

while the corrector step is

$$-\sigma_2 K_{3/2}^{n+1/2}\zeta_2^{n+1}+\left(C_1^{n+1/2}+\sigma_2 K_{3/2}^{n+1/2}\right)\zeta_1^{n+1}=C_1^{n+1/2}\zeta_1^n-\sigma_1 K_{3/2}^{n+1/2}+\sigma_1 K_{3/2}^n\left(\frac{\zeta_2^n-\zeta_1^n}{\Delta z}-1\right). \tag{A11}$$

A2.2. Upper Boundary

The upper boundary flux is calculated using the aforementioned daily precipitation rate (r_p) minus the evapotranspiration rate (r_e) (which is multiplied by the water content Θ at the top boundary so it can never exceed the available water). Thus, the surface flux $F=r_p-r_e\Theta_{n_z}$. Here Θ_{n_z} is used in lieu of $\Theta_{n_z+1/2}$ to avoid overshoots in extrapolation.

We use this given surface flux to simplify the equations near the upper boundary ($i=n_z$). The predictor step is

$$\left(C_{n_z}^n+\sigma_2 K_{n_z-1/2}^n\right)\zeta_{n_z}^{n+1/2}-\sigma_2 K_{n_z-1/2}^n\zeta_{n_z-1}^{n+1/2}=C_{n_z}^n\zeta_{n_z}^n+\sigma_1\left(F^n+K_{n_z-1/2}^n\right), \tag{A12}$$

while the corrector step is

$$\left(C_{n_z}^{n+1/2}+\sigma_2 K_{n_z-1/2}^{n+1/2}\right)\zeta_{n_z}^{n+1}-\sigma_2 K_{n_z-1/2}^{n+1/2}\zeta_{n_z-1}^{n+1}$$
$$=C_{n_z}^{n+1/2}\zeta_{n_z}^{n}+\sigma_1\left[F^{n+1/2}+K_{n_z-1/2}^{n+1/2}+F^{n}+K_{n_z-1/2}^{n}\left(\frac{\zeta_{n_z}^{n}-\zeta_{n_z-1}^{n}}{\Delta z}-1\right)\right]. \tag{A13}$$

The model is able to simulate surface ponding both by precipitation rates exceeding the infiltration capacity and by the water table rising above the surface. The infiltration excess is evaluated by estimating the maximum flux possible at each time step. Equation (10) is discretized numerically as

$$F_m=K_s\left(1-\frac{2\zeta_{n_z}}{\Delta z}\right), \tag{A14}$$

where the pressure term (ζ_{n_z}) is located at $z=H-\Delta z/2$. If the input flux at the surface in the predictor or corrector step is greater than this maximum flux, $F > F_m$, then we add the excess, $(F-F_m)\Delta t/2$, to the incoming flux at the next time step and set the current flux to the maximum, $F = F_m$. (NB: our unit of time is 1 day; otherwise the excess would need to be divided by the length of the day to give a flux.) The ponding has not been limited in these simulations.

A3. Boussinesq Equation

We also use a predictor-corrector formulation for the Boussinesq equation, following Pikul et al. (1974) but using the variable $b \equiv h^2$ to solve equation (11) for all internal horizontal points, i, equally-spaced in x. Equation (11) with the b substitution is

$$\frac{1}{h}\frac{\partial b}{\partial t}=\frac{K_s}{s_y}\frac{\partial^2 b}{\partial x^2}+2(S-D_r). \tag{A15}$$

The discretized predictor version of the equation is

$$\frac{K_s}{s_y}\frac{b_{i+1}^{n+1/2}-2b_i^{n+1/2}+b_{i-1}^{n+1/2}}{\Delta x^2}+2(S^n-D_r)-\frac{1}{h_i^n}\frac{(b_i^{n+1/2}-b_i^n)}{(\Delta t/2)}=0. \tag{A16}$$

The source/sink term S^n is kept constant throughout the time step. Using the constant

$$\sigma_3=\frac{K_s\Delta t}{2s_y\Delta x^2}, \tag{A17}$$

we can rearrange the predictor step into the tridiagonal formula

$$\sigma_3 h_i^n b_{i+1}^{n+1/2}-\left(1+2\sigma_3 h_i^n\right)b_i^{n+1/2}+\sigma_3 h_i^n b_{i-1}^{n+1/2}=-(S^n-D_r)h_i^n\Delta t-b_i^n. \tag{A18}$$

The corrector step is

$$\frac{K_s}{2s_y}\left[\frac{b_{i+1}^{n+1}-2b_i^{n+1}+b_{i-1}^{n+1}}{\Delta x^2}+\frac{b_{i+1}^{n}-2b_i^{n}+b_{i-1}^{n}}{\Delta x^2}\right]+2(S^n-D_r)-\frac{1}{h_i^{n+1/2}}\frac{b_i^{n+1}-b_i^n}{\Delta t}=0 \tag{A19}$$

which we can rearrange as

$$\sigma_3 h_i^{n+1/2}b_{i+1}^{n+1}-\left(1+2\sigma_3 h_i^{n+1/2}\right)b_i^{n+1}+\sigma_3 h_i^{n+1/2}b_{i-1}^{n+1}$$
$$=-2(S^n-D_r)h_i^{n+1/2}\Delta t-b_i^n-\sigma_3 h_i^{n+1/2}\left(b_{i+1}^n-2b_i^n+b_{i-1}^n\right). \tag{A20}$$

At the near-river boundary, $i = n_x$, a Dirichlet boundary condition is used to specify the height of the water in the river channel as $h_{n_x}=h_r(t)$. The predictor and corrector steps for the river boundary calculation $i=n_x-1$ are the same as given in (A18) and (A20), after replacing h_{n_x} by h_r and b_{n_x} by h_r^2.

The horizontal spatial extent of the model is chosen large enough so that the far-river boundary does not interfere with the water table dynamics in the area of interest near the channel. For this reason the far-river boundary, at $x = 0$ or $i = 0$ is specified to have a zero flux (or Neumann) boundary condition. For accuracy, near $x = 0$, b is expanded in a quadratic polynomial. The quadratic Taylor/MacLaurin Series expansion of h is

$$h(x)=h_0+\alpha x+\beta x^2, \tag{A21}$$

where h_0 is the unknown value of h at $x = 0$. Zero flux requires that at $x = 0$,

$$\frac{\partial h}{\partial x}(x=0)=0 \Rightarrow \alpha=0. \tag{A22}$$

We obtain h_0 from the known values of h at grid points $i = 1$ and 2, giving

$$h_0=\frac{4}{3}h_1-\frac{1}{3}h_2. \tag{A23}$$

This term can then be used to replace h_0 when $i = 1$ in equations (A18) and (A20).

A3.1. Evaluating the Source/Sink Term

The source/sink term, S, is calculated by calculating the materials balance of the water in the domain. This calculation is carried out at the vertical evaluation site along the x axis. As a default this is half way between the river channel and the inner-floodplain boundary. This simplification incurs some error because the extent of the vadose zone is defined by the x- dependent position of the water table. A more accurate solution would calculate the x-dependent materials balance by calculating $S(x, t)$ throughout the lateral domain. This however would be more computationally intensive.

The materials balance calculation is defined by

$$S=\frac{\text{change in vadose zone water content-change in the surface water input}}{\text{time step}\times\text{specific yield}}, \tag{A24}$$

where the change in vadose water content is calculated from

$$\Delta\theta\Delta z\sum_{i=1}^{n_z}\left(\Theta_i^{n+1}-\Theta_i^n\right) \tag{A25}$$

in which Θ_i^n is the nondimensional soil saturation at the end of time step n at grid point i. The change in surface water input is

$$\frac{\Delta t}{2}\left(F^n+F^{n+1/2}\right) \tag{A26}$$

with F^n representing the incoming flux at time step n. So the flux F_{wt} at the top of the water table into the phreatic zone is

$$F_{wt}=\frac{\Delta\theta\Delta z}{\Delta t}\sum_{i=1}^{n_z}\left(\Theta_i^{n+1}-\Theta_i^n\right)-\frac{1}{2}\left(F^n+F^{n+1/2}\right). \tag{A27}$$

Finally, the source/sink term is the phreatic zone influx scaled by the capacity or specific yield s_y of the soil:

$$S=F_{wt}/s_y. \tag{A28}$$

Appendix B: Evapotranspiration Calculation

B1. Evapotranspiration Equation

The Penman-Monteith equation (Monteith, 1965; Penman, 1948) calculates the evapotranspiration rate as a function of the amount of energy incident on a region, the mass transfer gradient (wind and relative humidity), and the canopy conductance (for transpiration). The full equation is given by

$$ET=\frac{\Delta(R_{ns}+R_{nl})+\gamma K_E\rho_w\lambda_v v_a e_a^*(1-W_a)}{\rho_w\lambda_v[\Delta+\gamma(1+C_{at}/C_{can})]}. \tag{B1}$$

Here Δ is the slope of the saturation-vapor versus temperature curve (kPa K^{-1}). The net radiation is calculated using R_{ns} and R_{nl} which are the net shortwave and incoming longwave radiation, respectively (MJ m^{-2} d^{-1}).

In the second part of the numerator, γ is the psychrometric constant (kPa K^{-1}). The remainder of this part calculates the mass transfer gradient using: K_E, a coefficient that reflects the efficiency of vertical transport of water vapor by the turbulent eddies of the wind (mkm^{-1} kPa^{-1}), ρ_w which is the mass density of water (999.97 kg m^{-3}), λ_v which is the latent heat of water vaporization (2.47 MJ kg^{-1}), v_a the wind speed (km

d^{-1}), e_a^* the saturation-vapor pressure at the air temperature (kPa) and, W_a which is the relative humidity of the air.

Finally, in the denominator, C_{at} and C_{can} are the atmospheric and canopy conductances, respectively. Equation (B1) is based on the assumptions that there is no ground-heat conduction or water-advected energy, and heat-energy storage remains constant (Dingman, 2015). Appendix B2 describes the methods used to calculate each of the climate parameters from equation (B1), and Appendix B3 describes the calculation of the transpiration parameters.

B2. Climate Parameters

To calculate daily evaporation using equation (B1), the following parameters are required: Δ, R_{ns}, R_{nl}, γ, K_E, ρ_w, λ_v, v_a, e_a^*, and W_a. These can be calculated using the latitude (ϕ in decimal degrees) and altitude (z_{alt} in m) of the site along with the following climate values for a given day n_{day} of that year's total number of days n_{year} (365 or 366): the maximum temperature (T_{max} in °C), the minimum temperature (T_{min} in °C), the dewpoint temperature (T_{dew} in °C), the atmospheric pressure at the station (P in kPa), the mean pressure at sea level (P_0 in kPa), and the average wind speed (v_a in km d^{-1}). The equations presented below have been sourced from Dingman (2015) unless stated otherwise.

The slope of the relationship between saturation-vapor pressure and temperature, Δ, can be calculated in kPa K^{-1} using the following equation:

$$\Delta = \frac{2508.3}{(T_{mean}+237.3)^2}\exp\left(\frac{17.3T_{mean}}{T_{mean}+237.3}\right), \tag{B2}$$

where T_{mean} is the average daily temperature in °C.

The methods for calculating the solar radiation have been taken from Allen et al. (1998). The net radiation incident on the surface in MJ m^{-2} d^{-1} is the sum of the net shortwave radiation, S, and incoming longwave radiation, L. First, we need the extraterrestrial radiation (R_a in MJ m^{-2} d^{-1}), which is calculated using only the location of the site

$$R_a = \frac{1440}{\pi}G_{sc}d_r[\omega_s\sin(\varphi)\sin(\delta)+\cos(\varphi)\cos(\delta)\sin(\omega_s)] \tag{B3}$$

In this equation, G_{sc} is a solar constant (0.0820 MJ m^{-2} min^{-1}), d_r is the inverse relative distance between the Earth and Sun, calculated by

$$d_r = 1+0.033\cos\left(\frac{2\pi}{365}n_{day}\right), \tag{B4}$$

and δ is the solar declination

$$\delta = 0.409\sin\left(\frac{2\pi}{365}n_{day}-1.39\right). \tag{B5}$$

ω_s is the sunset hour angle, defined by the following equation:

$$\omega_s = \cos^{-1}[-\tan(\varphi)\tan(\delta)], \tag{B6}$$

where φ is the latitude in radians.

The incoming solar radiation (R_s in MJ m^{-2} d^{-1}) can be inferred from this extraterrestrial radiation, along with the maximum and minimum temperature readings, using the Hargreages and Samani [1982] radiation formula

$$R_s = k_{Rs}\sqrt{T_{max}-T_{min}}R_a \tag{B7}$$

which is a function of k_{Rs}, an adjustment coefficient. Allen (1997) produced the following relation for k_{Rs}

$$k_{Rs} = k_{Ra}\sqrt{(P/P_0)}, \tag{B8}$$

where k_{Ra} is 0.17 for inland regions and P_0 is the mean pressure at sea level.

The net solar radiation is then found by

$$R_{ns}=(1-a)R_s, \tag{B9}$$

where a is the albedo. A typical grassland albedo is 0.107 (Dingman, 2015).

The clear-sky solar radiation, R_{so} can be calculated using the extraterrestrial radiation (R_s) and the site elevation above sea level (z_{alt}, m)

$$R_{so}=(0.75+2\text{x}10^{-5}z_{alt})R_a. \tag{B10}$$

We are then able to calculate the incoming longwave radiation using

$$R_{nl}=\sigma\left[\frac{(T_{max}+273.16)^4+(T_{min}+273.16)^4}{2}\right](0.34-0.14\sqrt{e_a})\left(1.35\frac{R_s}{R_{so}}-0.35\right), \tag{B11}$$

where σ is the Stefan-Boltzmann constant (4.903×10^{-9} MJ K^{-4} m^{-2} d^{-1}), and e_a is the actual vapor pressure in *kPa* (calculated later in this section).

In order to calculate the psychrometric constant, γ (kPa K^{-1}), the latent heat of vaporization is required λ_v (MJ kg^{-1}). This value is dependent on the temperature (°C) by the following relation:

$$\lambda_v=2.50-2.36\times10^{-3}T_{mean}. \tag{B12}$$

We can then use the heat capacity of air ($c_a=1\times10^{-3}$MJ kg^{-1} K^{-1}) along with the atmospheric pressure, P in kPa, to calculate the psychrometric constant by

$$\gamma\equiv\frac{c_aP}{MW_{ratio}\lambda_v}. \tag{B13}$$

MW_{ratio} is the ratio of the molecular mass of water vapor to dry air (0.622).

K_E is a coefficient that describes the ability of the wind to move water vapor by turbulent eddies. It can be calculated in mkm^{-1} kPa^{-1} for the liquid-vapor transition by

$$K_E\equiv\frac{0.622\rho_a}{P\rho_w}\frac{1}{6.25\left[\ln\left(\frac{z_m-z_d}{z_o}\right)\right]^2}, \tag{B14}$$

where ρ_a is the density of air (kg m^{-3}), ρ_w is the density of water (kg m^{-3}), z_m is the height at which wind speed and air vapor pressure are measured (m), z_d is the zero-place displacement (m), and z_0 is the roughness height of the surface (m).

The density of air can be calculated using the ideal gas law

$$\rho_a=\frac{1000P}{R_{specific}(T_{mean}+273.15)}, \tag{B15}$$

where $R_{specific}$ is the specific gas constant for dry air (287.058 Jkg^{-1} K^{-1}). For a bare soil, the zero-plane displacement is 0 and the roughness height can be taken as 0.001 m (Garratt & Hicks, 1973 cited in Haghighi and Or, 2015). We can assume the wind speed and air vapor pressure readings were taken from a height of 2 m.

Using the methods presented by Allen et al. (1998), the saturation-vapor pressure (e° in kPa) is related to the air temperature by the following equation:

$$e^\circ(T)=0.610\exp\left[\frac{17.27T}{T+237.3}\right]. \tag{B16}$$

The mean saturation-vapor pressure which is required for the evaporation equation can then be calculated by

$$e_a^*=\frac{e^\circ(T_{max})+e^\circ(T_{min})}{2}. \tag{B17}$$

In order to calculate the relative humidity from the known parameters we need the actual vapor pressure ($e_a=e^\circ(T_{dew})$). The fractional relative humidity can then be calculated by (Allen et al., 1998)

Table C1
*Soil Profile ed199 Sand, Silt, and Clay Content With Respective van Genuchten Parameter (to Four Decimal Places)s Calculated Using the ROSETTA Model (*Schaap et al., 2001*)*

Depth (m)	Sand (%)	Silt (%)	Clay (%)	Texture class	θ_r (m^3/m^3)	θ_s (m^3/m^3)	a (1/m)	n (N/A)	K_s (m/d)
0.01	39.9	24.1	36.0	Clay loam	0.0820	0.4240	1.9643	1.3110	0.0537
0.05	42.8	22.4	34.8	Clay loam	0.0802	0.4174	2.0864	1.3065	0.0602
0.15	44.8	20.7	34.5	Clay loam	0.0794	0.4133	2.2060	1.2978	0.0667
0.35	29.9	23.2	46.9	Clay	0.0908	0.4545	2.0249	1.2581	0.1085
0.75	26.3	25.4	48.3	Clay	0.0922	0.4635	1.8828	1.2633	0.1288
1.25	39.9	20.9	39.2	Clay loam	0.0841	0.4264	2.1928	1.2779	0.0638
1.75	64.0	11.0	25.0	Sandy clay loam	0.0659	0.3806	2.7536	1.3077	0.1472
2.55	45.3	20.0	34.7	Sandy clay loam	0.0794	0.4125	2.2537	1.2930	0.0691

$$W_a = \frac{e_a}{e_a^*}. \tag{B18}$$

B3. Transpiration Parameters

The transpiration parameters needed for equation (B1) are C_{at} and C_{can}. The atmospheric conductance can be calculated by

$$C_{at} = \frac{u(z_m)}{6.25\left[\ln\left(\frac{z_m - z_d}{z_0}\right)\right]^2}, \tag{B19}$$

where u is the wind speed, z_d is the displacement height, z_0 is the roughness height, and z_m can be taken as 2 m above the top of the vegetation canopy, z_{veg}. The values for grassland taken from Dingman (2015) are $z_d = 0.2$, $z_0 = 0.04$, and $z_m = 2 + z_{veg} = 2.6$. The canopy conductance is calculated using

$$C_{can} = k_s LAI C_{leaf}, \tag{B20}$$

where k_s is a shelter factor, LAI is the leaf-area index, and C_{leaf} is the leaf conductance. Dingman (2015) recommends a shelter factor (which accounts for some plants being sheltered from the sun and wind) of 0.5 for vegetated land. Grassland has a LAI of 0.7 to 2.6 and maximum leaf conductance of 50 m/s (Dingman, 2015). In the present study, we use the average grassland LAI of 1.65.

Appendix C: van Genuchten Parameters

The sand, silt, and clay percentages and van Genuchten parameters for the full soil profiles ("ed199" and "ed200") used in the study are provided in Tables C1 and C2. The sand, silt, and clay percentages were used to calculate the van Genuchten parameters using the ROSETTA model. The soil profile averages used as input to the model are provided in Table 2.

Table C2
*Soil Profile ed200 Sand, Silt, and Clay Content With Respective van Genuchten Parameters (to Four Decimal Places) Calculated Using the ROSETTA Model (*Schaap et al., 2001*)*

Depth (m)	Sand (%)	Silt (%)	Clay (%)	Texture class	θ_r (m^3/m^3)	θ_s (m^3/m^3)	a (1/m)	n (N/A)	K_s (m/d)
0.01	17.8	31.8	50.4	Clay	0.0965	0.4833	1.6293	1.2835	0.1597
0.05	31.0	28.0	41.0	Clay	0.0875	0.4466	1.7045	1.3104	0.0691
0.15	29.4	28.3	42.3	Clay	0.0887	0.4512	1.6939	1.3056	0.0778
0.35	25.7	29.7	44.6	Clay	0.0911	0.4612	1.6410	1.3014	0.0961
0.65	29.1	30.0	40.9	Clay	0.0881	0.4505	1.5926	1.3225	0.0751
0.75	30.5	30.1	39.4	Clay loam	0.0867	0.4462	1.5751	1.3314	0.0686
1.25	29.9	27.7	42.4	Clay	0.0886	0.4502	1.7290	1.3017	0.0767
2.55	16.6	27.3	56.1	Clay	0.0981	0.4903	1.8281	1.2434	0.2125

Appendix D: Numerical Sensitivity

The spatial step differs between the vertical infiltration and lateral exchange equations. For the (vertical) Richards equation, we consider an idealized domain of total soil depth H down to an impermeable layer divided into

$$n_z = \frac{NH}{\sqrt{K_s/(\alpha\lambda\Delta\theta)}} \tag{D1}$$

equal layers in z (nearest integer is implied). For the (horizontal) Boussinesq equation, we consider a domain width W to be twice the distance from the river channel to the vertical soil profile being modeled, divided into

$$n_x = \frac{NW}{\sqrt{K_s H/s_y}} \tag{D2}$$

equal intervals in x. Here N is the number of grid points used to resolve one characteristic diffusion length. By trial and error, $N = 60$ has been adopted in the results presented.

The time step is required to be the same in both equations to allow alternation of the calculations of each equation at each step. As a result, to accurately resolve the diffusive processes in both of the equations, the time step was chosen as the minimum value of the following options

$$\Delta t = c\min\left[\frac{\Delta z^2\alpha\lambda\Delta\theta}{K_s}, \frac{\Delta z\Delta\theta}{K_s}, \frac{\Delta x^2 s_y}{K_s H}\right], \tag{D3}$$

where $c = 0.5$, $\Delta x = W/n_x$, and $\Delta z = H/n_z$. The first and last terms ensure the diffusion processes are accurately resolved, while the middle term ensures that the vertical conduction is resolved. The choice of time step balances accuracy and efficiency. To demonstrate the accuracy, simulations were run at half time steps ($\Delta t/2$) which were found to have a negligible impact on the results. Moreover, the uncertainties involved in the input data and parameters were orders of magnitude higher than the differences resulting from time step alterations.

Appendix E: Calibration Details

The calibration methods and a discussion of the results for each of the 24 settings are provided in Appendix E1. The evaluation results for each set of paired parameters are listed in Appendix E2. Finally, Appendix E3 provides a discussion of the best practice for calibration identified by performance trends.

E1. Methods and Results

Two codes were created to automate the calibration process. The first (in Fortran 90) calculates the calibration parameters (difference in variability and difference in running average) for the available time period, by comparing the simulation output and piezometer data. The second code, written in Python, controls the iterative process of calculating the optimal K_s and D_r values. The Python code reads the initial K_s and D_r values and uses the Fortran code to generate the calibration parameters. It then reruns the simulation for incremental values of K_s until the sign of the difference in variability changes. A linear interpolation of the K_s values either side of a 0 difference in variability is then taken. This process is repeated with K_s values closer and closer to 0 until the difference from the previous K_s value is within a user-chosen threshold (see below). Then the optimal K_s value is used to conduct the same incremental changes and interpolations for the D_s value.

The years 2013 and 2014 were used as calibration periods. The 2 years were chosen because they have data available for all sites and are two distinct hydrological years, allowing a range of comparisons to be made. The initial K_s and D_r values used for all the calibrations were 1.0 and 0.0, respectively. Increments of K_s and D_r were set to initially be 1.0 and 0.01, respectively, and threshold differences were 0.005 and 0.00005, respectively. This means the K_s solution will be accurate up to three decimal places, as the calibration will run until the last two K_s solutions will be within 0.005 of each other, either side of a "0" difference in variability. Similarly, the D_r solution will be accurate up to five decimal places. Note that a K_s value of 0 is unphysical, so if $K_s < 1$ is required, then the value will step down by factors of 10 until the sign of vd changes.

For each calibration period, the simulation was run from the previous 1 July. This meant that the spin-up, along with the initial half-year of data would make the water table levels perfectly representative at any

distance from the river channel, no matter the K_s and D_r values at the start of the calibration period. The number of grid divisions in x (n_x) was kept constant throughout the calibration and chosen to be the solution to equation (D2) when $K_s = 1$. This meant that for solutions below $K_s = 1$ the n_x was less than the equation-recommended amount. However, since the $N = 60$ value in the equation was chosen as a very conservative value, when a select few outputs were compared with higher n_x counterparts, the differences were well below the K_s calibrated accuracy, so deemed insignificant. For reference, the n_x values used were: 212 for Old Mollee 50 m, 568 for Old Mollee 140 m, 1,325 for Old Mollee 320 m, 168 for Yarral East 40 m, 462 for Yarral East 110 m, and 1,231 for Yarral East 290 m.

The calibration was also run based on two different model setups; simulations based solely on the uncoupled lateral flow component and coupled simulations that included the vadose zone dynamics. The uncoupled version used no source/sink term or capillary fringe to represent water exchange with the vadose zone. This comparison was made both because the vadose zone component is not calibrated so may incorporate an unknown error, and also to indicate the effect of including interzone exchange. The six sites, two years and two model setups led to 24 different calibration combinations, the results of which are provided in Table E1.

In general, the further the site is located from the river, the higher the calibrated hydraulic conductivity (with the exception of the Old Mollee 50 m site). As the lateral hydraulic conductivity determines how quickly input variations translate across the floodplain, this finding is logical. Sites nearer the river do not require as high K_s values for variations to reach them when compared with similar variations much further away from the river channel. The overall difference between the 2013 and 2014 calibrations is not pronounced. In 8 out of the 12 sites, the 2013 calibrated hydraulic conductivity is higher than 2014 (but only by up to 0.4 m/d). The higher 2013 K_s values may be because the river stage inputs are more variable in 2013 so require a higher K_s to translate this variability into the floodplain. The exceptions are Old Mollee 50 m in both cases, Yarral East 110 m uncalibrated, and Old Mollee 320 m calibrated. Hence the differences are not pronounced or consistent enough to be certain of a pattern.

Table E1
Calibration Results for the Uncoupled and Coupled Code, for the Years 2013 and 2014, and for all Six Sites, Using the Automated Calibration Codes

Coupled?	Year	Site	K_s (m d^{-1})	vd	D_r (m)	yd
No	2013	Old Mollee 50 m	1.973	9.94×10^{-4}	0.11010	$<1 \times 10^{-7}$
No	2013	Old Mollee 140 m	0.937	1.28×10^{-4}	0.00680	-1.40×10^{-6}
No	2013	Old Mollee 320 m	2.592	1.64×10^{-5}	0.00204	-1.80×10^{-5}
No	2013	Yarral East 40 m	0.347	2.60×10^{-4}	−0.00020	$<1 \times 10^{-7}$
No	2013	Yarral East 110 m	0.864	5.00×10^{-5}	−0.00076	$>-1 \times 10^{-7}$
No	2013	Yarral East 290 m	2.935	7.40×10^{-6}	0.00045	-2.90×10^{-6}
No	2014	Old Mollee 50 m	2.265	6.39×10^{-4}	0.12957	1.00×10^{-7}
No	2014	Old Mollee 140 m	0.869	8.09×10^{-5}	0.00901	-2.00×10^{-7}
No	2014	Old Mollee 320 m	2.412	2.32×10^{-5}	0.00359	-2.69×10^{-5}
No	2014	Yarral East 40 m	0.298	2.82×10^{-5}	−0.00138	1.00×10^{-7}
No	2014	Yarral East 110 m	1.014	6.69×10^{-3}	0.00025	-1.00×10^{-7}
No	2014	Yarral East 290 m	2.550	2.07×10^{-5}	0.00198	-1.47×10^{-5}
Yes	2013	Old Mollee 50 m	4.558	7.33×10^{-4}	0.26775	2.00×10^{-7}
Yes	2013	Old Mollee 140 m	2.279	-4.39×10^{-4}	0.02968	$>-1 \times 10^{-7}$
Yes	2013	Old Mollee 320 m	4.898	-6.20×10^{-4}	0.01707	-3.90×10^{-6}
Yes	2013	Yarral East 40 m	0.778	8.85×10^{-5}	0.01352	-6.61×10^{-5}
Yes	2013	Yarral East 110 m	2.047	-1.99×10^{-4}	0.01244	-2.03×10^{-5}
Yes	2013	Yarral East 290 m	5.756	-6.85×10^{-4}	0.01568	-2.94×10^{-5}
Yes	2014	Old Mollee 50 m	5.498	4.19×10^{-4}	0.32570	-1.00×10^{-7}
Yes	2014	Old Mollee 140 m	2.117	-2.43×10^{-4}	0.02996	-6.90×10^{-6}
Yes	2014	Old Mollee 320 m	5.068	-1.75×10^{-4}	0.01537	-4.00×10^{-7}
Yes	2014	Yarral East 40 m	0.692	6.43×10^{-5}	0.00684	1.00×10^{-7}
Yes	2014	Yarral East 110 m	1.802	-1.37×10^{-4}	0.01064	-8.00×10^{-7}
Yes	2014	Yarral East 290 m	5.355	-1.98×10^{-4}	0.01314	-1.10×10^{-6}

Note. The hydraulic conductivity, K_s, the difference in variability vd ($vd = v_{mod} - v_{obs}$), the drainage term D_r and the average difference in running average yd (equation (14)) are listed for each calibration.

The uncoupled calibrations yielded much lower hydraulic conductivities and lower drainage terms than the coupled calibrations. This is because the source/sink term dampens the variability of the water table by drawing water into the unsaturated zone to lower peaks and infiltrating water from the unsaturated zone to reduce trough sharpness. Hence, a higher hydraulic conductivity is needed than without the unsaturated zone coupling, to maintain the variability. This higher hydraulic conductivity leads to a higher overall water table, as water propagates quickly into the floodplain so is able to maintain its elevation. Hence a higher drainage term than without the coupling is needed, to shift the water table elevations downward into the right range of values. NB: the drainage term is subtracted from the Boussinesq equation, therefore a higher drainage term leads to lower water table elevations.

E2. Evaluation

The exhaustive lists of evaluation parameters (R^2, NSE, and PBIAS) based on each of the paired calibrated parameters applied to each of the sites based (24 different combinations run on each of the six sites) are provided in Tables E2–E4, respectively.

E3. Results Discussion

For easy comparison, the evaluation parameters were combined to distinguish the relative performance of different sites, years and model setups in Table E5. As the evaluation parameters are all on different scales, the performance of a given calibration cannot be judged by summing the results across all evaluation parameters. The level of accuracy according to the R^2 value is determined by its magnitude, hence the R^2 values are best compared by summing the results for each calibration option. Again by summing, the NSE results are compared for each calibration. Finally, the modulus of the PBIAS values can be summed for comparison but, contrary to the other two parameters, the lowest values indicate the best performance. Table E5 shows the sum of each evaluation parameter for each calibration category, along with the number of

Table E2
R^2 Evaluation Results for Each of the 24 Pairs of Calibrated Parameters (Each Row) Applied to Each of the Six Sites (Each Column)

Coupled?	Year	Site	OM50	OM140	OM320	YE40	YE110	YE290
No	2013	OM50	0.884	0.757	0.660	0.868	0.884	0.909
No	2013	OM140	0.744	0.579	0.039	0.870	0.913	0.280
No	2013	OM320	0.922	0.803	0.450	0.864	0.878	0.887
No	2013	YE40	0.489	0.144	0.059	0.837	0.761	0.841
No	2013	YE110	0.725	0.558	0.009	0.870	0.912	0.020
No	2013	YE290	0.935	0.813	0.520	0.862	0.869	0.911
No	2014	OM50	0.903	0.773	0.698	0.866	0.879	0.919
No	2014	OM140	0.727	0.551	0.115	0.869	0.909	0.518
No	2014	OM320	0.914	0.795	0.402	0.865	0.883	0.872
No	2014	YE40	0.445	0.087	0.581	0.826	0.707	0.703
No	2014	YE110	0.762	0.611	0.016	0.871	0.917	0.178
No	2014	YE290	0.921	0.801	0.441	0.864	0.879	0.883
Yes	2013	OM50	0.964	0.807	0.779	0.853	0.836	0.950
Yes	2013	OM140	0.906	0.779	0.395	0.866	0.885	0.082
Yes	2013	OM320	0.968	0.821	0.690	0.852	0.826	0.953
Yes	2013	YE40	0.700	0.511	0.232	0.868	0.899	0.575
Yes	2013	YE110	0.892	0.769	0.271	0.868	0.893	0.770
Yes	2013	YE290	0.974	0.817	0.735	0.849	0.811	0.946
Yes	2014	OM50	0.972	0.805	0.779	0.850	0.821	0.953
Yes	2014	OM140	0.896	0.769	0.351	0.867	0.889	0.002
Yes	2014	OM320	0.969	0.821	0.702	0.851	0.823	0.950
Yes	2014	YE40	0.672	0.465	0.197	0.865	0.893	0.616
Yes	2014	YE110	0.873	0.749	0.182	0.869	0.900	0.682
Yes	2014	YE290	0.971	0.820	0.683	0.850	0.818	0.951
	Days available		1,462	1,456	1,461	912	912	912

Note. Each row represents the model performance for a calibration pair (K_s and D_r) applied to each of the six sites. The calibration settings are listed in the left-hand columns. For example the last entry in the first row is the R^2 result for the Yarral East 290 m site when the K_s and D_r terms were calculated based on the uncoupled 2013 Old Mollee 50 m calibration. The worst results are when $R^2 < 0.33$ the best results when $R^2 > 0.66$.

Table E3
NSE Evaluation Results for Each of the 24 Pairs of Calibrated Parameters (Each Row) Applied to Each of the Six Sites (Each Column)

Coupled?	Year	Site	OM50	OM140	OM320	YE40	YE110	YE290
No	2013	OM50	0.874	−4.150	−369.228	0.566	−10.255	−1257.869
No	2013	OM140	0.572	0.210	−0.566	0.761	0.578	−2.513
No	2013	OM320	0.779	0.486	−0.431	0.665	0.660	−4.655
No	2013	YE40	0.147	−2.646	−20.534	0.671	−6.461	−76.631
No	2013	YE110	0.505	−0.374	−7.908	0.747	−0.538	−40.778
No	2013	YE290	0.792	0.500	−0.474	0.650	0.632	−4.787
No	2014	OM50	0.897	−4.604	−401.029	0.535	−11.428	−1350.808
No	2014	OM140	0.565	0.272	−0.208	0.768	0.706	−2.796
No	2014	OM320	0.771	0.487	−0.288	0.674	0.689	−3.867
No	2014	YE40	0.033	−4.094	−79.232	0.599	−10.269	−132.294
No	2014	YE110	0.560	−0.106	−4.991	0.745	−0.020	−27.649
No	2014	YE290	0.776	0.480	−0.467	0.667	0.659	−4.862
Yes	2013	OM50	0.963	−5.476	−439.233	0.418	−14.156	−1468.827
Yes	2013	OM140	0.810	0.605	−4.468	0.682	0.623	−17.842
Yes	2013	OM320	0.851	0.691	0.431	0.593	0.613	0.925
Yes	2013	YE40	0.562	0.359	−3.199	0.778	0.888	−44.862
Yes	2013	YE110	0.763	0.561	0.148	0.695	0.822	0.693
Yes	2013	YE290	0.855	0.694	0.520	0.575	0.566	0.939
Yes	2014	OM50	0.972	−5.693	−451.689	0.390	−14.810	−1510.581
Yes	2014	OM140	0.802	0.580	−5.541	0.690	0.600	−24.139
Yes	2014	OM320	0.851	0.687	0.483	0.589	0.603	0.946
Yes	2014	YE40	0.490	0.055	−0.722	0.773	0.316	−3.007
Yes	2014	YE110	0.737	0.515	0.146	0.709	0.826	0.291
Yes	2014	YE290	0.851	0.681	0.504	0.583	0.586	0.893
	Days available		1,462	1,456	1,461	912	912	912

Note. The row title gives the calibration settings and the column title gives the simulation site. NSE < 0 indicates poor results while NSE > 0.5 indicates favorable results.

NSE values < 0 and the overall rank of each calibration category. This allows us to understand which calibration options perform best and to what extent they perform well. Along with the comparative evaluation results, the best and worst possible values for each calibration setting are shown for reference.

In Table E5, the three sections allow us to compare: the performance of each site, the two calibration years, and the coupled or uncoupled-model setups. The maximum number of available days was used for evaluation at each of the sites but the sample size varied depending on the completeness of the piezometer data set. The number of days used for each evaluation was 1,462 days for Old Mollee 50 m, 1,456 days for Old Mollee 140 m, 1,461 days at Old Mollee 320 m, and 912 days for each of the Yarral East sites. The two locations (Old Mollee and Yarral East) were not compared due to distinct differences in data set size. However, the different distances from the river within each of the locations have a similar number of days available so can be compared fairly. Clearly, the sites furthest from the river performed best.

Looking at the detailed results in Appendix E2, the sites closer to the river (especially the closest site Yarral East 40 m) are less sensitive to the calibration parameters, so lower values of hydraulic conductivity in the automated calibration will suffice for a good match. Hence, the further, more sensitive sites produce the highest hydraulic conductivities and calibrations that perform best overall. Since these were calibrated to have the highest hydraulic conductivities, we can conclude that calibrating based on sites closer to the river results in an under-estimation of the floodplain connectivity. Therefore, the furthest sites available should be used for calibration.

The Old Mollee 50 m site calibrations, which were exceptions in many of the trends identified during the calibration process (see section 3.2), performs poorly in the NSE and PBIAS tests. However, unexpectedly, the R^2 result is favorable. Little can be concluded from the interyear comparison. 2013 performs better in the R^2 and PBIAS results but worse in NSE, and both years produce the same number of simulations with NSE values < 0. Moreover, looking at the full results in Appendix E2, improved performance does not match up with any trends seen in the calibrated K_s values.

Table E4
PBIAS Evaluation Results for Each of the 24 Pairs of Calibrated Parameters (Each Row) Applied to Each of the Six Sites (Each Column)

Coupled?	Year	Site	OM50	OM140	OM320	YE40	YE110	YE290
No	2013	OM50	−0.016	0.963	8.196	0.083	0.678	6.748
No	2013	OM140	−0.164	−0.205	−0.276	−0.022	−0.118	−0.242
No	2013	OM320	−0.157	−0.181	−0.371	−0.014	−0.072	−0.448
No	2013	YE40	−0.242	−0.736	−1.934	−0.085	−0.584	−1.633
No	2013	YE110	−0.188	−0.392	−1.196	−0.039	−0.246	−1.214
No	2013	YE290	−0.158	−0.184	−0.392	−0.014	−0.072	−0.454
No	2014	OM50	−0.010	1.010	8.541	0.088	0.712	6.993
No	2014	OM140	−0.158	−0.160	0.002	−0.018	−0.092	0.149
No	2014	OM320	−0.157	−0.173	−0.325	−0.014	−0.068	−0.414
No	2014	YE40	−0.267	−0.903	2.381	−0.105	−0.675	−2.166
No	2014	YE110	−0.180	−0.330	−0.952	−0.032	−0.197	−1.003
No	2014	YE290	−0.158	−0.182	−0.378	−0.015	−0.073	−0.456
Yes	2013	OM50	0.002	1.100	8.940	0.097	0.783	7.292
Yes	2013	OM140	−0.127	0.061	0.926	0.006	0.086	0.804
Yes	2013	OM320	−0.144	−0.084	0.111	−0.004	0.002	0.031
Yes	2013	YE40	−0.144	−0.046	0.724	−0.009	−0.022	−1.206
Yes	2013	YE110	−0.147	−0.095	0.097	−0.008	−0.020	−0.034
Yes	2013	YE290	−0.145	−0.093	0.063	−0.005	−0.002	−0.002
Yes	2014	OM50	0.005	1.120	9.066	0.099	0.799	7.395
Yes	2014	OM140	−0.125	0.076	1.023	0.008	0.095	0.927
Yes	2014	OM320	−0.145	−0.092	0.070	−0.005	−0.003	0.003
Yes	2014	YE40	−0.169	−0.236	−0.271	−0.027	−0.155	0.018
Yes	2014	YE110	−0.150	−0.114	0.015	−0.010	−0.035	−0.110
Yes	2014	YE290	−0.146	−0.102	0.008	−0.006	−0.009	−0.045
	Days available		1,462	1,456	1,461	912	912	912

Note. The row title gives the calibration settings and the column title gives the simulation site. Values are expressed as a percentage with best values being when $|PBIAS| < 0.1$ and worst values when $|PBIAS| > 1$.

From Table E5, we can see that the coupled calibrations perform far better across most of the categories than the uncoupled calibrations. The NSE sum is the exception, but there are far fewer results with NSE values < 0 in the coupled calibrations. The higher overall NSE sum is attributed to disproportionately poor results from the Old Mollee 50 m output based on the furthest site calibrations. Hence, the coupled calibrations perform best, with Old Mollee 50 m being the exception. Therefore, despite the fact that the infiltration component of the model remains uncalibrated, including the dynamics of the unsaturated zone is

Table E5
Sum of the Evaluation Parameters for Each of the Calibration Options for Comparison (NB: the Highest Values Indicate Best Performance Except for the PBIAS Values, for Which the Modulus of the Values is Summed and the Lowest Values Indicate Best Performance)

Calibration setting	$\sum R^2$	$\sum$ NSE	# NSE < 0	$\sum$ |PBIAS|	Rank
OM50	20.370	−7314.222	16	70.734	5
OM140	14.802	−48.252	8	5.870	3
OM320	19.761	4.232	4	3.088	1
YE40	13.973	−378.281	12	14.702	6
YE110	15.166	−72.902	8	6.804	4
YE290	19.924	2.814	4	3.161	2
Best/worst values	**24/0**	**24/−∞**	**0/24**	**0/∞**	**1/6**
2013	51.919	−3779.443	26	52.142	1
2014	52.078	−4027.169	26	52.219	2
Best/worst values	**72/0**	**72/−∞**	**0/72**	**0/∞**	**1/2**
Uncoupled	49.275	−3828.136	36	58.218	2
Coupled	54.722	−3978.475	16	46.142	1
Best/worst values	**72/0**	**72/−∞**	**0/72**	**0/∞**	**1/2**

Note. The following abbreviations are used in the table Old Mollee (OM), Yarral East (YE), 50 m (50), etc.

Table E6
Sum of the Evaluation Parameters for all Six Sites Based on Each of the Best Six Calibrations

Category	$\sum R^2$	$\sum$ NSE	# NSE < 0	$\sum$ |PBIAS|	Rank
Coupled 2013 YE290	5.132	4.150	0	0.310	1
Coupled 2014 OM320	5.116	4.158	0	0.318	2
Coupled 2014 YE290	5.094	4.098	0	0.315	3
Coupled 2013 OM320	5.110	4.103	0	0.377	4
Coupled 2013 YE110	4.464	3.682	0	0.401	5
Coupled 2014 YE110	4.255	3.222	0	0.435	6
Best/worst values	**6/0**	**6/$-\infty$**	**0/6**	**0/∞**	**1/24**

Note. The highest values indicate best performance except for the PBIAS values, for which the modulus of the values is summed and the lowest values indicate best performance.

crucial to the model's performance. This indicates the great importance of the interzone exchange and relationship between the two zones in capturing the patterns of water table movement.

The evaluation parameters for the six best calibrations, which are also the only calibrations that have no NSE values < 0, are summarized in Table E6. We can see that all the best sites are all based on the coupled calibration, starting with the furthest sites.

Acknowledgments
We would like to thank Sébastien Lamontagne and Andrew Taylor from the Commonwealth Scientific and Industrial Research Organisation (CSIRO) Land and Water in Australia for their provision of and advice with the groundwater monitoring and soil parameter data for the Murray-Darling basin. The authors would also like to thank the editor Jean Bahr and three anonymous reviewers for their detailed and constructive evaluation of the work which was very helpful and encouraging. Evans would also like to acknowledge the generous funding provided by the Natural Environment Research Council (NERC) and the University of St Andrews 600 Fund, without which this work would not have been possible. Singer was supported by funding from NSF EAR #700555. The sources of each data input are provided throughout the paper. The data output files are hosted online by the NERC Environmental Information Data Centre (Evans et al., 2018).

References

Allen, R. G. (1997). Self-calibrating method for estimating solar radiation from air temperature. *Journal of Hydrologic Engineering*, *2*, 56–67.
Allen, R. G. Pereira, L. S., Raes, D., & Smith, M. (1998). *Crop evapotranspiration-guidelines for computing crop water requirements* (FAO Irrig. and Drain. Pap. 56). Rome, Italy: FAO.
Baird, A. J., & Wilby, R. L. (1999). *Eco-hydrology: Plants and water in terrestrial and aquatic environments*. Routledge, London: Psychology Press.
Boussinesq, J. (1904). Recherches théoriques sur l'écoulement des nappes d'eau infiltrées dans le sol et sur le débit des sources. *Journal De Mathématiques Pures Et Appliquées 5me Série*, *10*, 5–78.
Canham, C. A., Froend, R. H., Stock, W. D., & Davies, M. (2012). Dynamics of phreatophyte root growth relative to a seasonally fluctuating water table in a Mediterranean-type environment. *Oecologia*, *170*(4), 909–916.
CSIRO (2007). Water availability in the Namoi. A report to the Australian Government from the CSIRO Murray-Darling Basin Sustainable Yields Project (154 pp.). CSIRO, Australia.
Darcy, H. (1856). Les fontaines publique de la ville de Dijon (647 p.). Paris, France: Dalmont.
Diersch, H.-J., & Perrochet, P. (1999). On the primary variable switching technique for simulating unsaturated-saturated flows. *Advances in Water Resources*, *23*(3), 271–301.
Dingman, S. L. (2015). *Physical hydrology* (3rd ed.). Englewood Cliffs, NJ: Prentice Hall.
Doody, T. M., Colloff, M. J., Davies, M., Koul, V., Benyon, R. G., & Nagler, P. L. (2015). Quantifying water requirements of riparian river red gum (*Eucalyptus camaldulensis*) in the Murray-Darling Basin, Australia—Implications for the management of environmental flows. *Ecohydrology*, *8*(8), 1471–1487.
Ehleringer, J., & Dawson, T. (1992). Water uptake by plants: Perspectives from stable isotope composition. *Plant, Cell & Environment*, *15*(9), 1073–1082.
Evans, C. M., Dritschel, D. G., & Singer, M. B. (2018). Mathematically modelled daily water saturation profiles for sites on the Namoi River floodplain in south-east Australia at different distances from the river. Lancaster, UK: NERC Environmental Information Data Centre. https://doi.org/10.5285/5f2e06df-d141-4549-95b6-6a56300fc790
Evaristo, J., Jasechko, S., & McDonnell, J. J. (2015). Global separation of plant transpiration from groundwater and streamflow. *Nature*, *525*, 91– 94.
Feddes, R. A., Hoff, H., Bruen, M., Dawson, T., De Rosnay, P., Dirmeyer, P., et al. (2001). Modeling root water uptake in hydrological and climate models. *Bulletin of the American Meteorological Society*, *82*(12), 2797–2809.
Gat, J. R. (1996). Oxygen and hydrogen isotopes in the hydrologic cycle. *Annual Review of Earth and Planetary Sciences*, *24*(1), 225–262.
Haghighi, E., & Or, D. (2015). Linking evaporative fluxes from bare soil across surface viscous sublayer with the Monin-Obukhov atmospheric flux-profile estimates. *Journal of Hydrology*, *525*, 684–693.
Harbaugh, A. W., Banta, E. R., Hill, M. C., & McDonald, M. G. (2000). MODFLOW-2000, the U.S. geological survey modular ground-water model-user guide to modularization concepts and the ground-water flow process (Open-file Rep. 00–92, 134 p.). Reston, VA: U.S. Geological Survey.
Hargreages, G. H., & Samani, Z. A. (1982). Estimating potential evapotranspiration. *Journal of Irrigation and Drainage Engineering*, *108*(3), 225–230.
Harter, T., & Hopmans, J. W. (2004). *Role of vadose zone flow processes in regional scale hydrology: Review, opportunities and challenges*. Dordrecht, the Netherlands: Kluwer.
Ivkovic, K. M., Letcher, R. A., & Croke, B. F. W. (2009). Use of a simple surface-groundwater interaction model to inform water management. *Australian Journal of Earth Sciences*, *56*(1), 71–80.
Karssies, L. (2011). *CSIRO national soil archive and the national soil database (NatSoil). v1*. Canberra, Australia: CSIRO.
Kendall, C., & McDonnell, J. J. (2012). *Isotope tracers in catchment hydrology*. Amsterdam, the Netherlands: Elsevier.
Lamontagne, S., Taylor, A. R., Batlle-Aguilar, J., Suckow, A., Cook, P. G., Smith, S. D., et al. (2015). River infiltration to a subtropical alluvial aquifer inferred using multiple environmental tracers. *Water Resources Research*, *51*, 4532–4549. https://doi.org/10.1002/2014WR015663
Lamontagne, S., Taylor, A. R., Cook, P. G., Crosbie, R. S., Brownbill, R., Williams, R. M., et al. (2014). Field assessment of surface water-groundwater connectivity in a semi-arid river basin (Murray-Darling, Australia). *Hydrological Processes*, *28*, 1561–1572.

Lamontagne, S., Taylor, A., Cook, P. G., & Smithson, A. (2011). *Interconnection of surface and groundwater systems—River losses from losing/disconnected streams. Namoi River site report*. Adelaide, Australia: CSIRO Water for a Healthy Country National Research Flagship.

Maxwell, R. M., Kollet, S. J., Smith, S. G., Woodward, C. S., Falgout, R. D., Ferguson, I. M., et al. (2016). ParFlow User's Manual. Integrated Ground Water Modeling Center Report GWMI (167 pp.). Retrieved from https://inside.mines.edu/~rmaxwell/parflow.manual.2-15-16.pdf

Maxwell, R. M., Putti, M., Meyerhoff, S., Delfs, J. O., Ferguson, I. M., Ivanov, V., et al. (2014). Surface-subsurface model intercomparison: A first set of benchmark results to diagnose integrated hydrology and feedbacks. *Water Resources Research*, *50*, 1531–1549. https://doi.org/10.1002/2013WR013725

Monteith, J. (1965). Evaporation and environment. *Symposia of the Society for Experimental Biology*, *19*, 205–234.

Moriasi, D. N., Arnold, J. G., Liew, M. W. V., Bingner, R. L., Harmel, R. D., & Veith, T. L. (2007). Model evaluation guidelines for systematic quantification of accuracy in watershed simulations. *Transactions of the ASABE*, *50*(3), 885–900.

National Climatic Data Center (NCDC) (2017). *Global surface summary of the day—GSOD*. National Centers for Environmental Information (NCEI), U.S. Department of Commerce. Asheville, North Carolina. Retrieved from https://data.nodc.noaa.gov/cgi-bin/iso?id=gov.noaa.ncdc:C00516

Penman, H. L. (1948). Natural evaporation from open water, bare soil and grass. *Proceedings of the Royal Society A: Mathematical, Physical and Engineering Sciences*, *193*(1032), 120–145.

Pikul, M. F., Street, R. L., & Remson, I. (1974). A numerical model based on coupled one-dimensional Richards and Boussinesq Equations. *Water Resources Research*, *10*(2), 295–302.

Pittock, J., & Connell, D. (2010). Australia demonstrates the Planet's Future: Water and climate in the Murray Darling Basin. *International Journal of Water Resources Development*, *26*(4), 561–578.

Rassam, D. W., Peeters, L., Pickett, T., Jolly, I., & Holz, L. (2013). Accounting for surface-groundwater interactions and their uncertainty in river and groundwater models: A case study in the Namoi River, Australia. *Environmental Modelling and Software*, *50*, 108–119.

Refsgaard, J. C., & Storm, J. B. (1995). MIKE SHE. In Singh, V. P. (Ed.), *Computer models of watershed hydrology* (pp. 806–846). CO: Water Resource Publications.

Richards, L. A. (1931). Capillary conduction of liquids through porous mediums. *Journal of Applied Physics*, *1*, 318–333.

Rohde, M. M., Froend, R., & Howard, J. (2017). A global synthesis of managing groundwater dependent ecosystems under sustainable groundwater policy. *Ground Water*, *55*(3), 293–301.

Sargeant, C. I., & Singer, M. B. (2016). Sub-annual variability in historical water source use by Mediterranean riparian trees. *Ecohydrology*, *9*, 1328–1345. https://doi.org/10.1002/eco.1730

Schaap, M. G., Leij, F. J., & van Genuchten, M. T. (2001). Rosetta: A computer program for estimating soil hydraulic parameters with hierarchical pedotransfer functions. *Journal of Hydrology*, *251*(3), 163–176.

Šimůnek, J., van Genuchten, M. T., & Šejna, M. (2008). Development and applications of the HYDRUS and Stanmod software packages and related codes. *Vadose Zone Journal*, *7*(2), 587–600.

Singer, M., Sargeant, C., Piégay, H., Riquier, J., Wilson, R. J. S., & Evans, C. M. (2014). Floodplain ecohydrology: Climatic, anthropogenic, and local physical controls on partitioning of water sources to riparian trees. *Water Resources Research*, *50*, 4490–4513. https://doi.org/10.1002/2014WR015581

Singer, M. B., Stella, J. C., Dufour, S., Piégay, H., Wilson, R. J. S., & Johnstone, L. (2013). Contrasting water-uptake and growth responses to drought in co-occurring riparian tree species. *Ecohydrology*, *6*, 402–412.

Singh, V. P., & Woolhiser, D. A. (2002). Mathematical modeling of watershed hydrology. *Journal of Hydrologic Engineering*, *7*(4), 270–292.

Snyder, K. A., & Williams, D. G. (2000). Water sources used by riparian trees varies among stream types on the San Pedro river, Arizona. *Agricultural and Forest Meteorology*, *105*(1), 227–240.

Sprenger, M., Leistert, H., Gimbel, K., & Weiler, M. (2016). Illuminating hydrological processes at the soil-vegetation-atmosphere interface with water stable isotopes. *Reviews of Geophysics*, *54*(3), 674–704.

Taylor, A. R., Lamontagne, S., & Crosbie, R. S. (2013). Measurements of riverbed hydraulic conductivity in a semi-arid lowland river system (Murray-Darling Basin, Australia). *Soil Research*, *51*, 363–371.

Therrien, R., McLaren, R., Sudicky, E., & Panday, S. (2010). *Hydrogeosphere: A three-dimensional numerical model describing fully-integrated subsurface and surface flow and solute transport*. Waterloo, ON: Groundwater Simulations Group, University of Waterloo.

Van Dijk, A. I. J. M., Beck, H. E., Crosbie, R. S., De Jeu, R. A. M., Liu, Y. Y., Podger, G. M., et al. (2013). The Millennium Drought in southeast Australia (2001–2009): Natural and human causes and implications for water resources, ecosystems, economy, and society. *Water Resources Research*, *49*, 1040–1057. https://doi.org/10.1002/wrcr.20123

van Genuchten, M. T. (1991). Recent progress in modelling water flow and chemical transport in the unsaturated zone. In *20 th General Assembly of the International Union of Geodesy and Geophysics* (pp. 169–183), Vienna, Austria, 08/11–24/91.

Van Genuchten, M. T. (1980). A closed-form equation for predicting the hydraulic conductivity of unsaturated soils. *Soil Science Society of America Journal*, *8*(44), 892–898.

Williams, D., Scott, R., Huxman, T., Goodrich, D., & Lin, G. (2006). Sensitivity of riparian ecosystems in arid and semiarid environments to moisture pulses. *Hydrological Processes*, *20*(15), 3191–3205.

Zucker, M. B., Remson, I., Janet, E., & Aguado, E. (1973). Hydrologic studies using the Boussinesq equation with recharge term. *Water Resources Research*, *9*, 586–592. https://doi.org/10.1029/WR009i003p00586